Structural Effect on Electrochemical Performance of 4,4’-Biphenyldicarboxylate Sodium Salts as an Anode for Na-ion Batteries

Aram Choi

Department of Energy Engineering
(Battery Science and Technology)

Graduate School of UNIST

2014

Structural Effect on Electrochemical Performance of 4,4’-Biphenyldicarboxylate Sodium Salts as an Anode for Na-ion Batteries

Aram Choi

Department of Energy Engineering
(Battery Science and Technology)

Graduate School of UNIST

2014

Structural Effect on Electrochemical Performance of 4,4’-Biphenyldicarboxylate Sodium Salts as an Anode for Na-ion Batteries

A thesis
submitted to the Graduate School of UNIST
in partial fulfillment of the
requirements for the degree of
Master of Science

Aram Choi

02. 20. 2014
Approved by

Major Advisor
Kyu Tae Lee

Structural Effect on Electrochemical Performance of 4,4’-Biphenyldicarboxylate Sodium Salts as an Anode for Na-ion Batteries

Aram Choi

This certifies that the thesis of Aram Choi is approved.

02. 20. 2014

Signature

Thesis supervisor: Kyu Tae Lee

Signature

Hoi Ri Moon

Signature

Sung You Hong

Abstract

The crystal structures and electrochemical performance of 4,4'-biphenyldicarboxylate sodium salts is first introduced as an anode for Na-ion batteries. The structural modification of 4,4'-biphenyldicarboxylate sodium salts showing different degree of deprotonation and the coordination of a water molecule are deliberately accomplished through various precipitation and solvothermal methods, resulting in the formation of three different crystal structures even though they are composed of the same organic (bpdc) and inorganic (Na^+) building blocks. The crystal structures are determined by single-crystal X-ray diffraction. The powder X-ray diffraction patterns showed the good agreemen t with the corresponding simulated patterns, indicating that the phase pure powders have the same crystal structure as the single crystals. The level of deprotonation in 4,4'-biphenyldicarboxylate sodium salts affects not only electrochemical performance but also reaction mechanisms. The fully deprotonated 4,4'-biphenyldicarboxylate disodium salt (Na_2bpdc) exhibits promising electrochemical performance including reversible capacity of 220 mA h g^{-1} at ca. 0.5 V *vs.* Na/Na^+, negligible capacity fading over 150 cycles, and excellent rate performance delivering about 100 mA h g^{-1} even at a 20C rate, which is better than monosodium 4,4'-biphenyldicarboxylate (NaHb pdc) that is partially deprotonated. This better rate performance of Na_2bpdc salts is definitely attributed to the smaller particle size (short diffusion length) of that compared to NaHbpdc. However, even the dehydrated disodium 4,4'-biphenyldicarboxylate monohydrate (h-Na_2bpdc) having similar size to NaHbpdc exhibited better rate performance than NaHbpdc. This means that the rate performance is affected by the degree of deprotonation in 4,4'-biphenyldicarboxylate sodium salts. Carboxylic group causes the large amount of electrolyte decomposition to form thick solid electrolyte interphase (SEI) layers, resulting in the increase of polarization due to large charge-transfer resistance. Also, the de/sodiaiton of Na_2bpdc salts proceeds in a two-phase reaction, regardless of the degree of deprotonation. And, the amorphization of Na_2bpdc salts occurred during cycling, even though the crystal structure is maintained. However, unlike the fully deprotonated showing reversible phase transition during sodiation and desodiation, the partially deprotonated exhibits irreversible phase transition during cyclings. It seems to be occurred the partially phase transition to Na_2bpdc which is fully deprotonated due to the ion-exchange between Na^+ and H^+.

Contents

List of figures

Figure. 12 FT-IR spectra of H_2bpdc, *hyd*-Na_2bpdc, Na_2bpdc and NaHbpdc; all the spectra were measured by using attenuated total reflectance (ATR) technique.

Figure. 13 Voltage profiles of (a) NaHbpdc and (b) Na_2bpdc; cycle performance of (c) NaHbpdc and (d) Na_2bpdc

Figure 14. Voltage profiles of super P carbon.

Figure. 15 Rate performance of *hyd*-Na_2bpdc, Na_2bpdc and NaHbpdc

Figure. 16 Rate performance of NaHbpdc, h-Na_2bpdc, and Na_2bpdc: voltage profiles of (a) NaHbpdc, (b) h-Na_2bpdc, and (c) Na_2bpdc.

Figure. 17 SEM images of (a) NaHbpdc, (b) *hyd*-Na_2bpdc, and (c) Na_2bpdc

Fig. 18 Nyquist plots of bpdc electrode/bpdc electrode symmetric cells

Figure. 19 *Ex situ* XRD analysis of Na_2bpdc: (a) voltage profiles, (b) corresponding XRD patterns, and (c) XRD patterns of desodiated electrodes during the various cyclings.

Figure. 20 GITT curves of Na_2bpdc.

Figure. 21 *Ex situ* XRD analysis of NaHbpdc: (a) voltage profiles and (b) corresponding XRD patterns.

Figure 22. XRD patterns of NaHbpdc powders after storage in electrolytes for 3, 5, and 10 days.

List of tables

List of Schemes

1. Introduction

1.1. Lithium-ion batteries

For several decades, lithium ion batteries (LIBs) are considered the most efficient energy storage system and governed the market of electronic devices.[1-2] The lithium ion batteries are firstly commercialized in 1991 by Sony that are using $LiCoO_2$ for cathode and graphite for anode. $LiCoO_2$ showed quite good reversible capacity of 140 mAh/g which is deintercalated of Li ions up to 0.5Li and charged to 4.2V (*vs.* Li/Li^+). Graphite is theoretically reacted with one Li per six carbon, and appeared the 372 mAh/g theoretical capacity, 0~0.25V (*vs.* Li/Li^+). During charge process, Li ions, which are deintercalation from $LiCoO_2$ (cathode), migrate into graphite (anode) through an electrolyte. Discharge process is vice versa. Schematic illustration of the first Li-ion battery is showed in figure.1.[3]

After the commercialization of $LiCoO_2$ and graphite, lots of electrode materials are developed and researched to alternate these materials for LIB (figure.2).[4] As a structural perspective, cathode materials are mainly categorized into layered structure, spinel structure, and olivine structure materials. Firstly, layered structure materials are $LiCoO_2$, $LiNiO_2$, $LiNi_{0.5}Mn_{0.5}O_2$, and $LiNi_xCo_yMn_zO_2(x+y+z=1)$. $LiNiO_2$ has the higher reversible capacity than LiCoO2 and lower cost, so it is considered as an alternative to $LiCoO_2$. However, delithiated $LiNiO_2$ showed the safety problems due to structural instability, resulting in decomposition of oxide reacted with organic electrolytes. $LiNi_{0.5}Mn_{0.5}O_2$ exhibited the high reversible capacity of 200 mAh/g (2.5V~4.5V window *vs.* Li/Li^+) and also showed better thermal stability than other layered oxide materials ($LiCoO_2$, $LiNiO_2$). However, it showed cation disorder between the 3a and 3b sites due to the similar size of Ni^{+2} and Li^+, resulting in disturbance of Li diffusion. One of the most promising materials for commercialization is $LiNi_xCo_yMn_zO_2(x+y+z=1)$. This materials are compensating each metal's disadvantages, optimizing of each metal's advantages. Secondly, the spinel $LiMn_2O_4$ offers good safety and structural stability due to 3D lattice. Furthermore, Mn is low cost and environmentally friendly. Unfortunately, it showed severe problem that Mn dissolution into electrolytes resulting in deposition to anode. Thirdly, $LiFePO_4$ is polyanion-based cathode material of olivine structure. It has some advantages that thermal stability, low material cost, abundant material supply and better environmental compatibility. The disadvantages of $LiFePO_4$, however, indicate low theoretical capacity, low density, poor electronic and ionic conductivity.[2,4,5] Lithiated graphite has been the most commonly utilized lithium ion batteries anode material. To alternative graphite, many materials are researched as alkali metal-insertion host materials of carbonaceous compounds, alloy composites, metal oxides/sulfides, and organic compounds containing carbonyl groups.

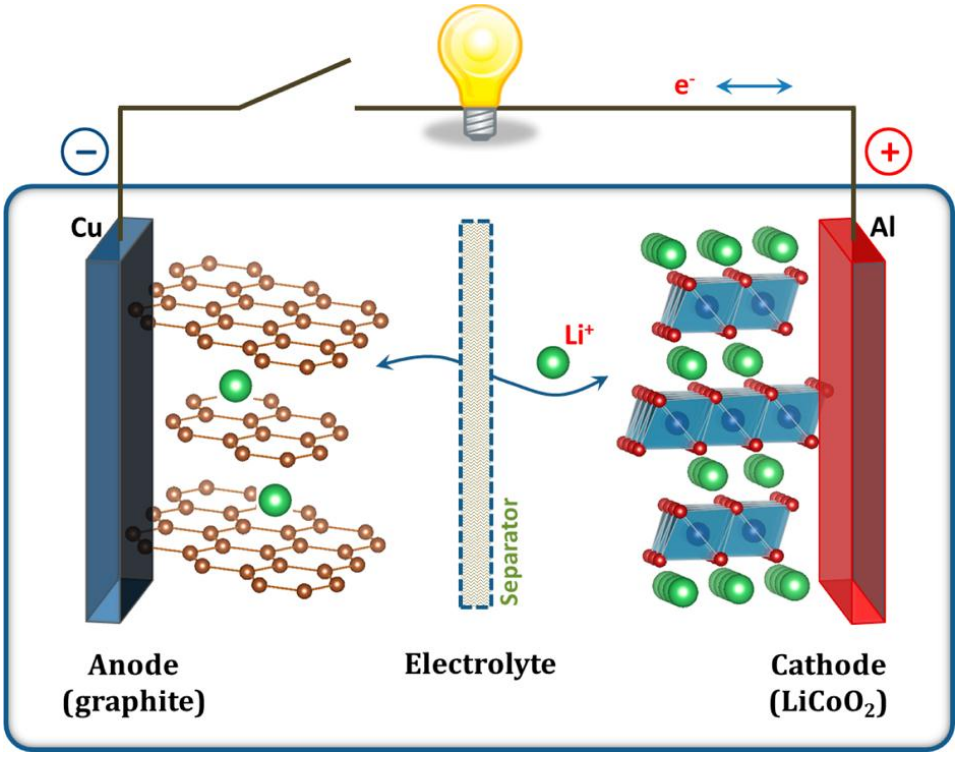

Figure. 1 Schematic illustration of the first Li-ion battery ($LiCoO_2$/Li^+ electrolyte/graphite).

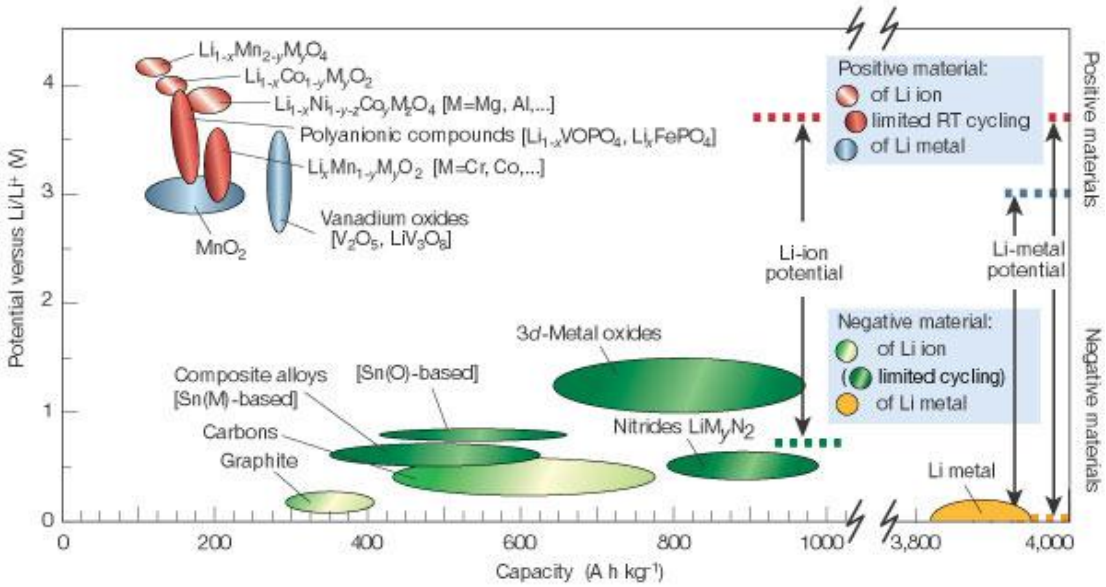

Figure. 2 Voltage versus capacity for positive- and negative-electrode materials presently used or under serious considerations for the next generation of rechargeable Li-based cells.

1.2. Sodium-ion batteries

Despite of the success of LIBs in portable electronics markets, their large scale applications (e.g., electric vehicles, the electrical grid system) have been limited due to performance and cost issues.[6] Since lithium resources are limited and geometrically constrained, world's growing demand for energy will eventually drive up the prices.[7] With the natural abundance, low toxicity, and low redox potential (-2.71 V vs SHE), sodium ion batteries (SIB) are considered one of the promising post-LIB systems that are cheap, environmentally benign, and sustainable. Moreover, sodium also belongs to alkali metals located directly below lithium on the periodic table. Therefore the similar synthetic or electrochemical approaches applied to LIBs could have been adapted to SIB system. For example, sodium analogues of cathodic materials have been synthesized including layered transition metal oxides ($NaMnO_2$, $NaCoO_2$) and polyanions ($NaFePO_4$).

However, the larger ionic radius of Na^+ (1.02 Å) causes structural changes of electrode materials and brings typically slow kinetics compared to Li^+ (0.76 Å) analogues. For example, sodium cation cannot intercalate into graphite, which is the representative anodic material of LIBs. Hard carbons with disordered structures have been tested for anodic applications to accommodate Na^+ ions, however, they showed inferior cyclabilities and specific capacities compared to graphite in LIBs.[8]

Lots of electrode materials are researched for sodium ion batteries, their voltage-capacity plots are shown in Figure.4.[9]

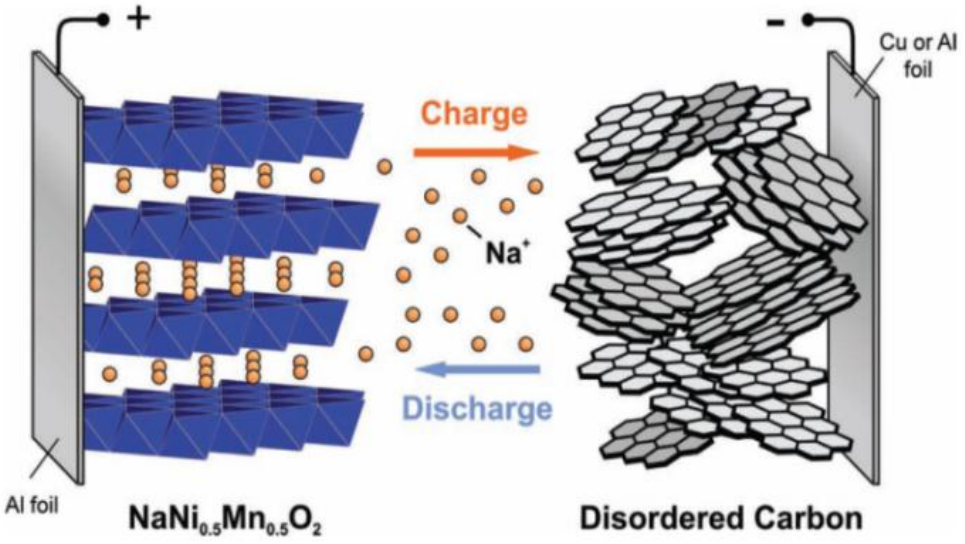

Figure. 3 Schematic illustration of sodium ion battery.[10]

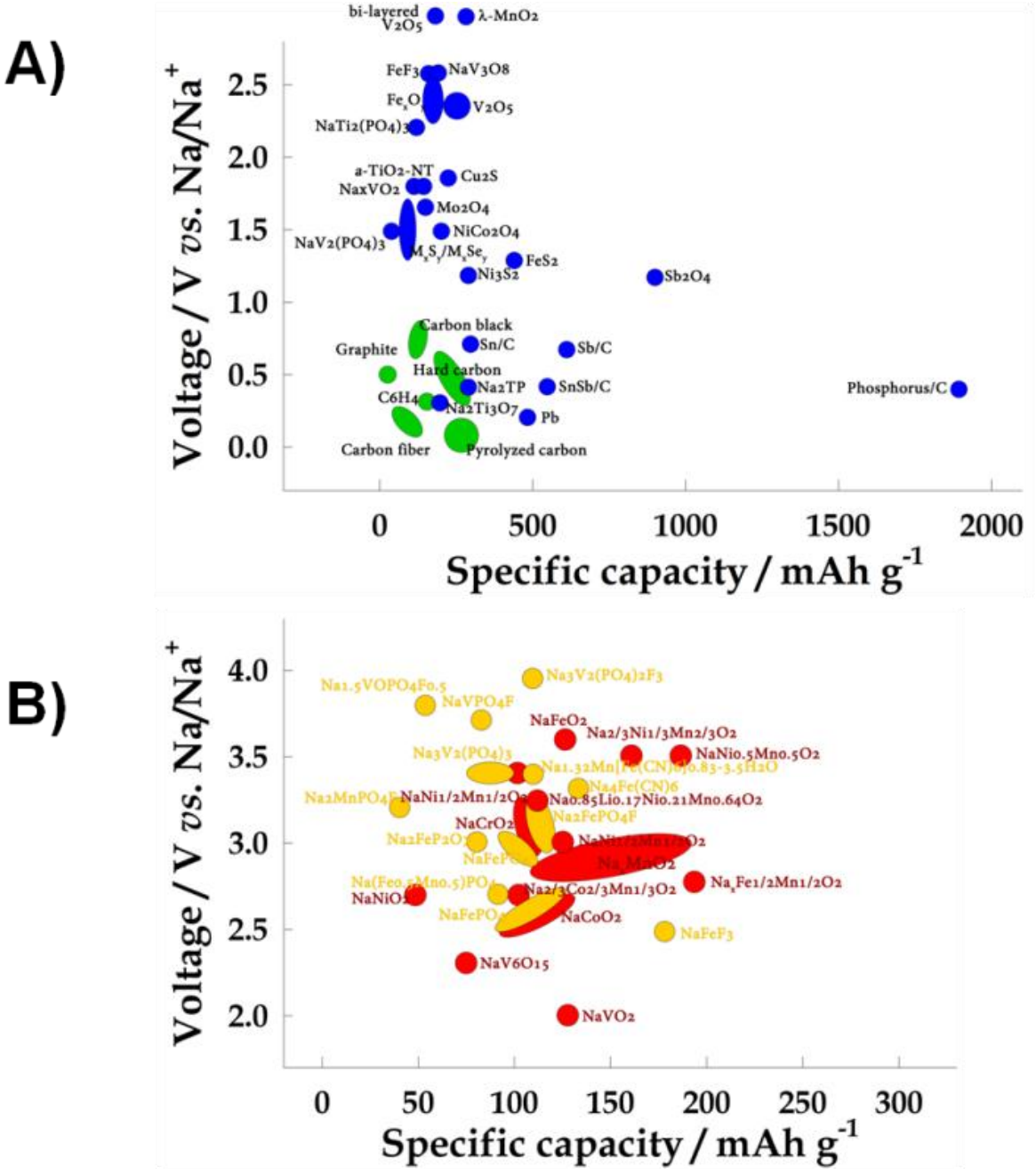

Figure. 4 Voltage-capacity plots of (A) negative and (B) positive electrode materials for SIBs.

1.3. Organic electrode materials

The history of organic compounds is as old as electrode materials for lithium ion batteries. However, they are not concerned comparing to inorganic electrode materials. Until now, lots of inorganic electrode materials are developed, but it is hard to find new inorganic electrode materials for both lithium ion batteries and sodium ion batteries. Organic compounds offer low-cost production, recyclability, and structural diversity. Especially, the structural richness of organic electrode materials give a lot of new electrode materials for both cathode and anode materials that can be easily tuned electrochemical properties and diversities. Organic compounds are categorized into organic sulfurs, disulfides, nitroxide radicals, and conjugated carbonyl derivatives (figure.5).[11]

Nonetheless, organic compounds have some challenges such as small volumetric capacity, low cyclability, and poor electrical conductivity.[9] In 2009, Tarascon et al. introduced conjugated dicarboxylate anodes (dilithium terephthalate, Li_2TP) for lithium ion batteries to solve those problems. It showed good electrochemical performance no other organic compounds which are large initial capacity of approximately 290 mAh/g, low redox potential of 0.8V vs. Li/Li^+, and stable cycle performance.[12]

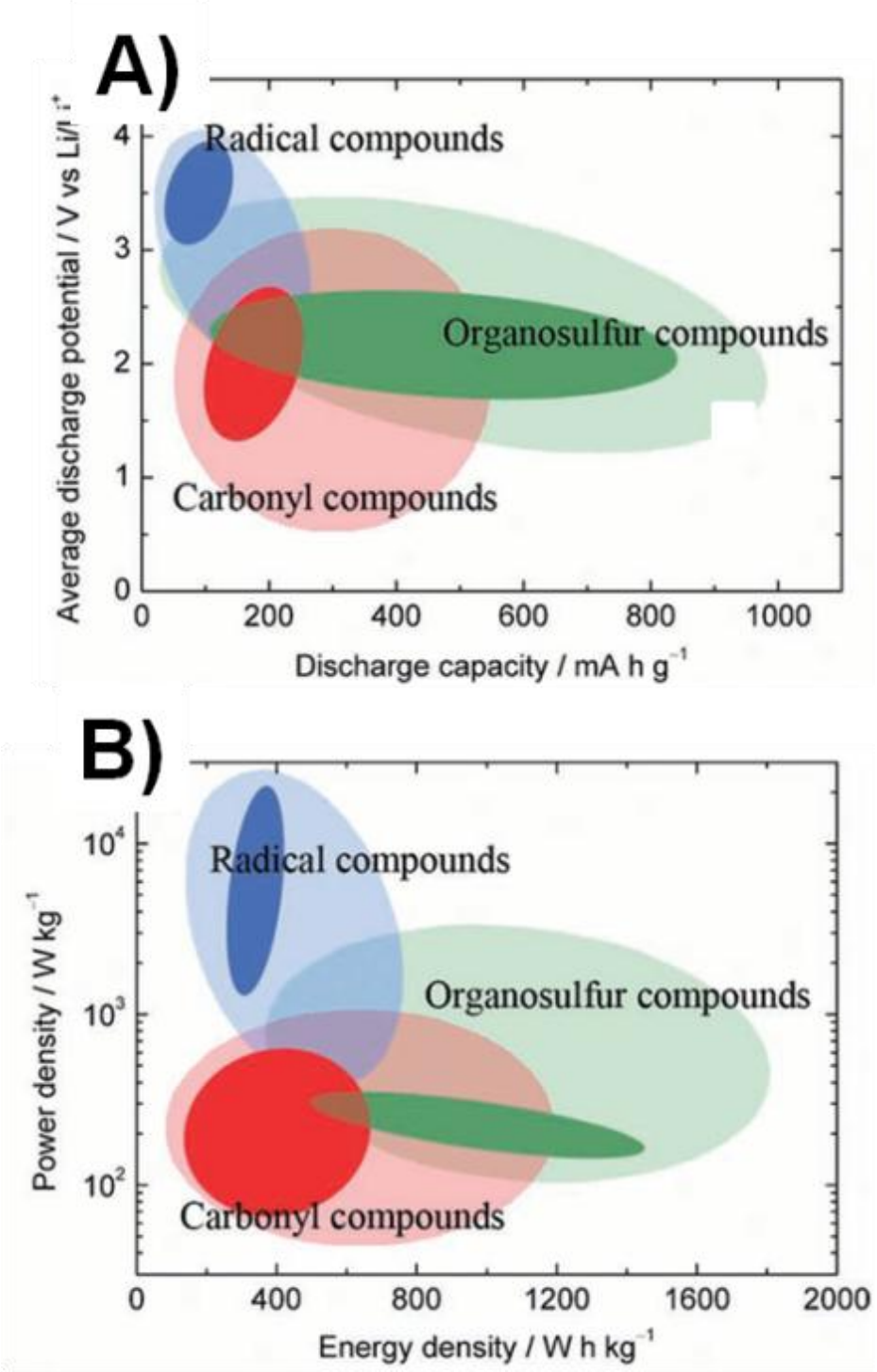

Figure. 5 Electrochemical performance of organic compounds for LIBs: (A) average discharge potential vs. discharge capacity plot and (B) power density vs. energy density plot.

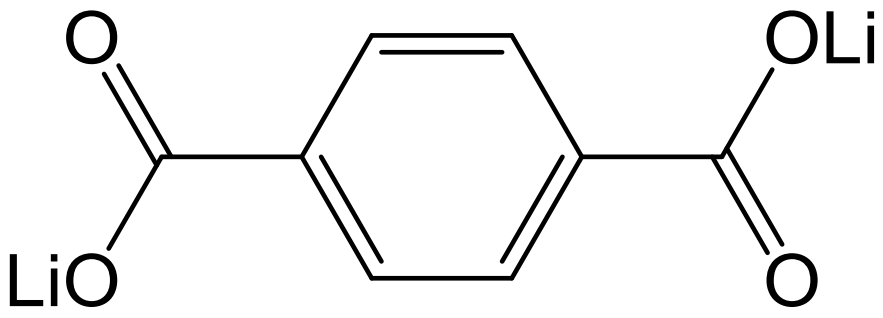

Figure. 6 Chemical structure of dilithium terephthalate

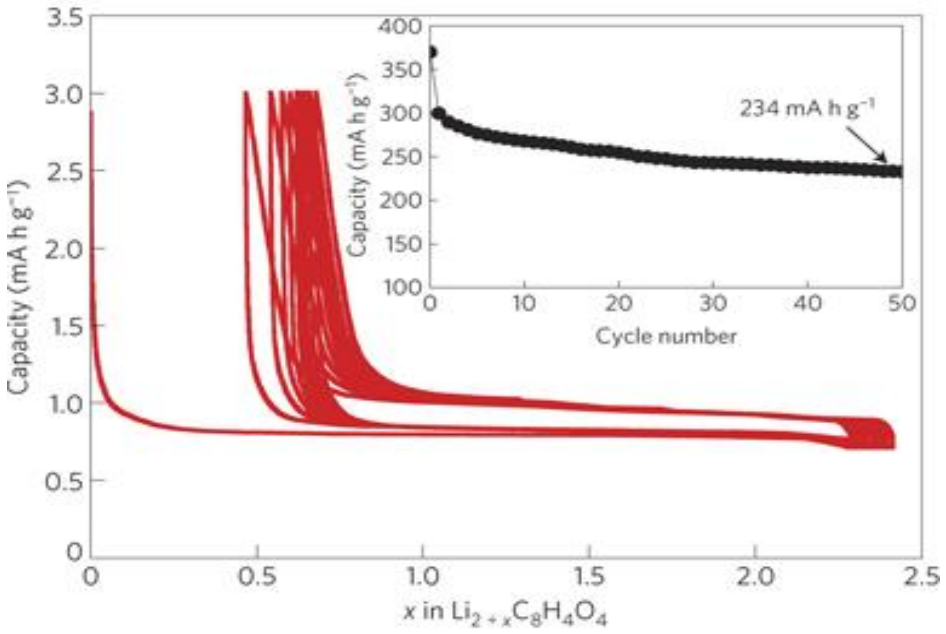

Figure. 7 Voltage profiles during initial 10 cycles and cycle performance (inset) of Li_2TP for li ion batteries

1.4. Organic anode materials for sodium-ion batteries

A variety of electrode materials such as non-graphitic carbons,[10,13,14] alloys (e.g., Sn and Sb),[15-18] metal oxides,[19-23] and phosphorus[24,25] have been shown to exhibit promising electrochemical performances as an anodes for Na-ion batteries. Recently, a few organic compound-based materials such as conjugated and aromatic compounds containing carbonyl groups or *N*-heterocycles have been reported as promising anode materials because of their attractive features such as good electrochemical performance, low-cost production, recyclability, and structural diversity.[12,26-30] For example, organic electrode materials can be produced from commonly used recycled materials such as polyethylene terephthalate (PET). In particular, disodium terephthalate (Na_2TP) were firstly introduced as organic anode materials for sodium ion batteries which has a space group of $Pbc2_1$. It showed remarkably excellent electrochemical properties. Na_2TP reversibly delivered about 250 mAh g^{-1} at about 0.4 V vs. Na/Na^+. It showed high capacity retention over 90 cycles with excellent (>98%) coulombic efficiency. Furthermore, Several sodium terephthalate derivatives with amino- and bromo-groups have been easily synthesized owing to the structural diversity of organic architecture, resulting in controllable redox potential changes through inductive and resonance effects.[31] Despite structural richness of organic electrode materials, even only a few organic compounds have been examined as Na-ion batteries.[32-34]

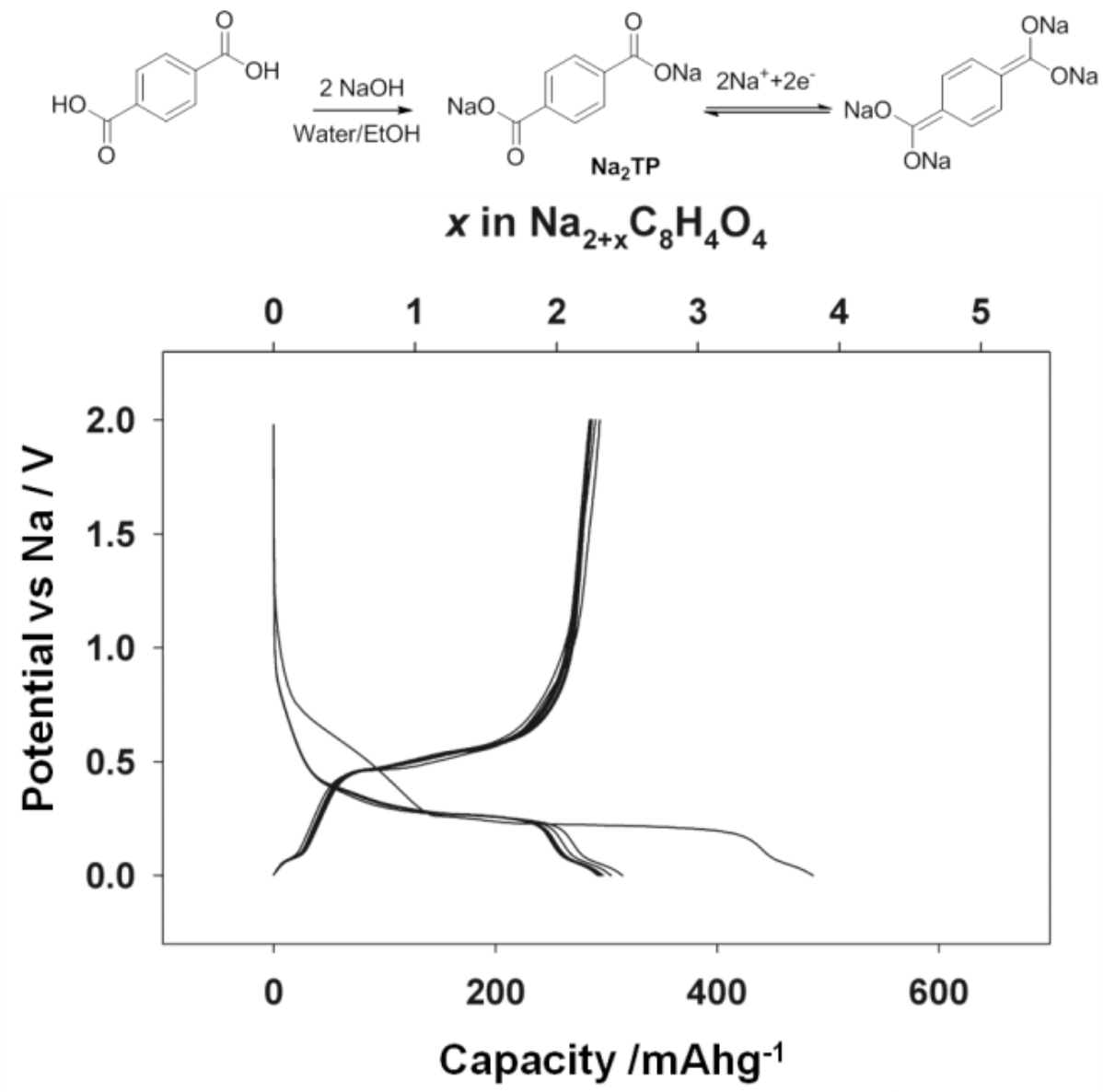

Figure. 8 Proposed reversible Na-ion insertion/deinsertion mechanism and voltage profiles.

2. Experimental

2.1. Synthesis method

[(Na_2bpdc)·H_2O]$_n$ (*hyd*-Na_2bpdc): To an aqueous suspension (3.2 mL) of 4,4'-biphenyldicarboxylic acid (H_2bpdc) (0.258 g, 1.06 mmol), an aqueous solution (0.8 mL) of NaOH (0.137 g, 3.43 mmol) was added. After the completion of the reaction, the solution was filtered, and the clear pale yellow filtrate was exposed to ethanol vapor inside a refrigerator (2 °C) to crystallize the products. After two days, block-shaped pale yellow single crystals of [(Na_2bpdc)·H_2O]$_n$ (h-Na_2bpdc) started to form at the surface of the solution. The crystals were filtered off after seven days, washed with ethanol, and dried in air. Yield: 0.17 g (53%). FT-IR (ATR): $\nu_{O\text{-}C=O(carboxylate)}$, 1579(s), 1 390(s); $\nu_{O\text{-}H(guest\ water)}$ cm^{-1}. Anal. calcd for $Na_2C_{14}H_{10}O_5$ (304.21): C, 55.27; H, 3.31. Found: C, 53.26; H, 3.27.

[(Na_2bpdc)]$_n$ (Na_2bpdc): To a stirred aqueous suspension (25 mL) of 4,4'-biphenyldicarboxylic acid (2.42 g, 0.01 mol), an aqueous solution (7 mL) of NaOH (1.20 g, 0.03 mol) was added. After the completion of the reaction, the solution was filtered, and ethanol (20 mL) was added to the filtrate, resulting in white precipitates. The solution was then allowed to stand in a refrigerator for several hours. The white precipitate obtained was filtered, washed with ethanol, and dried in air. Yield: 2.04 g (71%). ^{1}H-NMR (deuterium oxide): δ ppm 7.85 (d, 4H). 7.67 (d, 4H). FT-IR (ATR): $\nu_{O\text{-}C=O}$, 1578(s), 1394(s) cm^{-1}. Anal. calcd for $Na_2C_{14}H_8O_4$ (286.19): C, 58.76; H, 2.82. Found: C, 57.48; H, 2.84.

[NaHbpdc]$_n$ (NaHbpdc): $NaNO_3$ (0.026 g, 0.30 mmol) was dissolved in methanol (2 mL) and H_2bpdc (0.036 g, 0.15 mmol) was dissolved in DMA/H_2O (5.1 mL, 4:1.1 *v/v*). The two solutions were placed in a glass jar and sealed together, and the mixture was heated at 100 ℃ for 48 h. The solution was then cooled to room temperature. The plate-shaped colorless crystals obtained were filtered, washed briefly with methanol, and dried in air. Yield: 0.029 g (74%). FT-IR (ATR): $\nu_{C=O(carboxylic\ acid)}$, 1672 cm^{-1}; $\nu_{O\text{-}C=O(carboxylate)}$, 1605, 1399 cm^{-1}. Anal. calcd for $Na_1C_{14}H_9O_4$ (264.21): C, 63.64; H, 3.43. Found: C, 64.07; H, 3.88.

2.2. Characterization

All chemicals and solvents used in the syntheses were of reagent grade and they were used as received without further purification. The IR spectra were recorded using a ThermoFisher Scientific Nicolet 6700 FT-IR spectrophotometer. Elemental analyses (EA) were performed at the UNIST Central Research Facilities (UCRF) in Ulsan National Institute of Science and Technology (UNIST). Thermogravimetric analyses (TGA) were performed under N_2 (g) atmosphere at a scan rate of 5 ^oC/min using a Q50 (TA instruments). PXRD data were recorded using a Bruker D2 PHASER automated diffractometer at 30 kV and 10 mA for Cu Kα (λ = 1.54050 Å), with a step size of 0.02^o in 2θ. Scanning electron microscopy was carried out using a cold FE-SEM (Hitachi). Single crystals of *hyd*-Na_2bpdc and NaHbpdc, coated with Paratone-N oil, were mounted on a loop, and the diffraction data were collected at 95 K with synchrotron radiation (λ = 0.64999 Å for *hyd*-Na_2bpdc; 0.69999 Å for NaHbpdc) using a ADSC Quantum-210 detector at 2D SMC with a silicon (111) double crystal monochromator (DCM) at Pohang Accelerator Laboratory, S. Korea. The ADSC Q210 ADX program was used for the data collection, and HKL3000 (Ver. 703r) was used for the cell refinement, reduction, and absorption correction. The structures of *hyd*-Na_2bpdc and NaHbpdc have been deposited in the CCDC database, reference numbers 944127 and 944128, respectively.

2.3. Electrochemical measurements

The samples of electrochemically active materials (57.1 wt%) were mixed with carbon black (Super P, 28.6 wt%) and carboxymethyl cellulose (CMC, 14.3 wt%). The electrochemical performance was evaluated using 2032 coin cells with a Na metal anode and 0.8 M $NaClO_4$ in a mixture of ethylene carbonate and diethyl carbonate (1:1 v/v) electrolyte solution. The galvanostatic experiments were performed at 30^{o}C, and specific current densities of 18.7 mA g^{-1} (ca. 0.1 C) and 20.3 mA g^{-1} (ca. 0.1 C) were applied to evaluate the cycle performances of NaHbpdc and Na_2bpdc, respectively. For the rate performance evaluation, the discharging (desodiation) current density was fixed at 0.1 C, and the charging current was varied. The GITT experiments were performed between 0.1 and 2.5 V vs. Na/Na^+ by applying a current corresponding to a C/20 rate in intervals of 1 h, separated by a rest period of 1 h. The electrochemical impedance spectroscopy (EIS) study was performed using a BIO Logic SP 150. The AC impedance measurements were recorded using a signal with amplitude of 5 mV and a frequency range from 300 kHz to 1 mHz.

3. Results and discussion

H_2bpdc ligand and sodium cations were reacted under three different reaction conditions to afford three different types of bpdc-sodium salts. Disodium bpdc monohydrate (*hyd*-Na_2bpdc), $\{Na[Na(H_2O)](bpdc)\}_n$, was synthesized by the reaction of NaOH with H_2bpdc in water, and single crystals of the product were obtained by slow diffusion of ethanol at ca. 2 °C. NaOH was employed in this reaction as a source of Na ions and a strong base for deprotonating the carboxylic acid (COOH) groups of H_2bpdc. On the other hand, interestingly, non-hydrated disodium bpdc (Na_2bpdc) was synthesized as a microcrystalline solid by the rapid reaction of NaOH with H_2bpdc in a mixture of water and ethanol at room temperature. The partially deprotonated sodium salt, monosodium bpdc (NaHbpdc), $[Na(Hbpdc)]_n$, was synthesized by the solvothermal reaction of $NaNO_3$ and H_2bpdc in a mixture of methanol, *N*,*N*-dimethylacetamide (DMA), and water at 100 °C. Under these conditions, only one of two carboxylic acid (COOH) groups of H_2bpdc was deprotonated. Thus, the three bpdc-sodium salts were composed of the same organic (bpdc) and inorganic (Na^+) building blocks, but had different compositions and crystal structures.

Because *hyd*-Na_2bpdc and NaHbpdc could be obtained as single crystals, their crystal structures were directly determined and compared via single-crystal X-ray diffraction results. The lattice parameters, agreement factors, and detailed structural information of *hyd*-Na_2bpdc and NaHbpdc are listed in Table 1. *hyd*-Na_2bpdc crystallized in the monoclinic $P2_1/c$ space group. As shown in Figure. 9a, the structure of *hyd*-Na_2bpdc consisted of Na-O layers as the secondary building units (SBUs), and the bridging ligands, $bpdc^{2-}$, formed a three- dimensional (3D) network. The Na-O layers resulted from the coordination between Na^+ ions and O atoms of carboxylate groups (COO^-) and water molecules. The crystal structure of *hyd*-Na_2bpdc possessed two Na^+, two halves of $bpdc^{2-}$ ligand, and one coordinating water molecule, which are crystallographically independent. Figure. 9c reveals the coordination modes of carboxylates (COO^-) in *hyd*-Na_2bpdc to be as follows: the O1-C1-O2 group acts as a tetradentate ligand forming a four-membered chelate ring, and the O3-C8-O4 group coordinates to four Na ions without chelation. Na1 and Na2 exhibited a distorted trigonal bipyramidal and an octahedral coordination geometry, respectively. The $bpdc^{2-}$ ligand was planar with a dihedral angle of 0° between the two phenyl rings.

NaHbpdc crystallized in the triclinic P-*1* space group. The crystal structure of NaHbpdc showed two crystallographycally independent Na^+ ions and one $bpdc^{2-}$ ligand. The Na^+ ions were bridged by carboxylate groups (COO^-) to form one-dimensional (1D) Na-O chains as SBUs, which were linked by $bpdc^{2-}$ ligands to form a 3D network (Figure. 9b). Na1 and Na2 showed distorted octahedral and square

planar geometry, respectively. Unlike *hyd*-Na_2bpdc, the phenyl rings in the $bpdc^{2-}$ ligand of NaHbpdc were tilted by 30.69(5)°. Because the carboxylic acid (COOH) groups in NaHbpdc were partially depronated, the deprotonated O1-C1-O2 group coordinated to three Na ions using both the oxygen atoms. In contrast, only the O3 atom in O3-C8-O4-H44 acted as a bidentate ligand (Figure. 9d).

Table 1. X-ray crystallographic data of $\{Na[Na(H_2O)](bpdc)\}_n$ (h-Na_2bpdc) and $[Na(Hbpdc)]_n$ (NaHbpdc).

Compound	$\{Na[Na(H_2O)](bpdc)\}_n$	$[Na(Hbpdc)]_n$
formula	$Na_2C_{14}H_{10}O_5$	$Na_1C_{14}H_9O_4$
crystal system	*Monoclinic*	*Triclinic*
space group	*P 21/c*	*P-1*
fw	304.21	264.21
a, Å	27.720(6)	3.6550(7)
b, Å	5.8060(12)	11.214(2)
c, Å	7.5530(15)	12.985(3)
V, Å ^{3}	1214.2(4)	529.54(18)
Z	4	2
ρ_{calcd}, g cm^{-3}	1.665	1.657
temp , K	95(2)	100(2)
λ, Å	0.64999	0.69999
μ, mm^{-1}	0.185	0.156
goodness-of-fit (F^2)	1.037	1.003
F(000)	616	272
reflections collected	16907	5662
independent reflections	5223 [*R*(int) = 0.0448]	2827 [*R*(int) = 0.0307]
completeness to θ_{max}, %	98.6	93.2
data/parameters/restraints	5223/190/0	2827/179/0
θ range for data collection, deg	3.28-33.36	1.55-29.55
diffraction limits (*h*, *k*, *l*)	$-42\le h\le 41$, $-8\le k\le 8$, $-12\le l\le 12$	$-5\le h\le 5$, $-15\le k\le 15$, $-18\le l\le 18$
refinement method	Full-matrix least squares on F^2	Full-matrix least squares on F^2
R_1, wR_2 [$I>2\sigma(I)$]	0.0351[a], 0.0996[b]	0.0623[a], 0.1720[c]
R_1, wR_2 (all data)	0.0375[a], 0.1011[b]	0.0748[a], 0.1859[c]
largest peak, hole, eÅ $^{-3}$	0.870, -0.363	0.533, -0.887

[a] $R = \Sigma||F_O| - |F_C||/\Sigma|F_O|$. [b] $wR(F^2) = [\Sigma w(F_O^2 - F_C^2)^2/\Sigma w(F_O^2)^2]^{1/2}$ where $w = 1/[\sigma^2(F_O^2) + (0.0518P)^2 + (0.7461)P]$, $P = (F_O^2 + 2F_C^2)/3$. [c] $wR(F^2) = [\Sigma w(F_O^2 - F_C^2)^2/\Sigma w(F_O^2)^2]^{1/2}$ where $w = 1/[\sigma^2(F_O^2) + (0.1536P)^2 + (0.0000)P]$, $P = (F_O^2 + 2F_C^2)/3$.

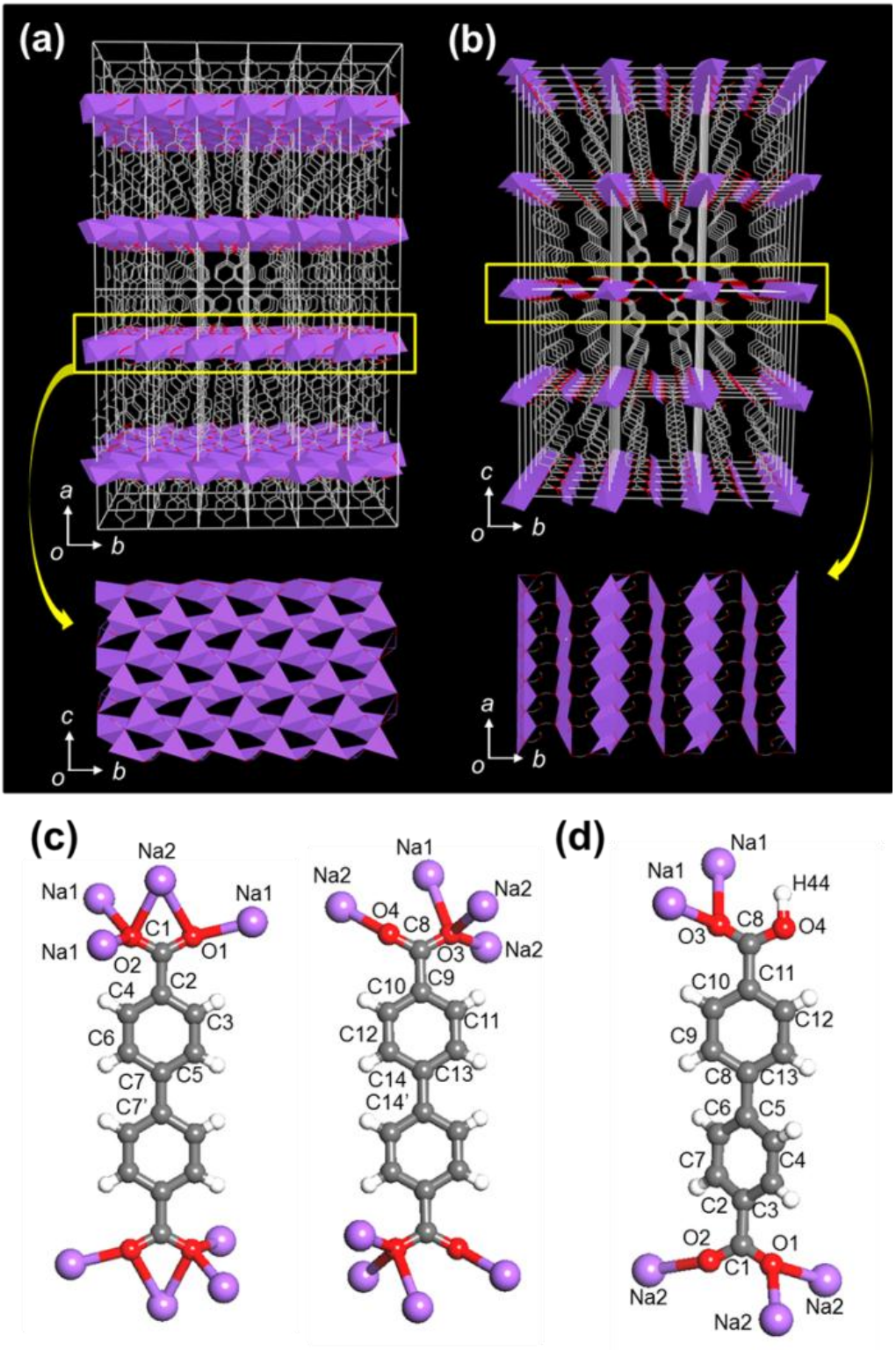

Figure. 9 Single-crystal X-ray structures of *hyd*-Na_2bpdc and NaHbpdc, which were constructed by connecting the SBUs (purple) by $bpdc^{2-}$ ligands. 3D network of (a) *hyd*-Na_2bpdc and (b) NaHbpdc; coordination modes of $bpdc^{2-}$ ligands to sodium ions in (c) *hyd*-Na_2bpdc, and (d) NaHbpdc. Color scheme: C (grey), O (red), H (white), Na (purple).

The PXRD patterns of the as-synthesized *hyd*-Na_2bpdc and NaHbpdc powders were compared to the simulated patterns based on the single crystal XRD data. As shown in Figures. 10a-d, the XRD patterns of both the bulk powders showed good agreement with the corresponding simulated patterns, indicating that the phase pure powders have the same crystal structure as the single crystals. On the other hand, because Na_2bpdc was obtained as microcrystals, which are not suitable for single crystal XRD analysis, its PXRD pattern (Figure. 10e) was compared to those of *hyd*-Na_2bpdc and NaHbpdc. Na_2bpdc showed a different PXRD pattern, indicating that the crystal structure of Na_2bpdc was different from those of *hyd*-Na_2bpdc and NaHbpdc. However, the structure of Na_2bpdc was found to be the same as that of *hyd*-Na_2bpdc after the coordinating water molecules were removed (Figure. 10f). *hyd*-Na_2bpdc was dehydrated by heating at 120 ^oC under vacuum. The dehydration results in a weight loss of 5.98% below 100 ^oC in the thermogravimetric analysis (TGA) curves of *hyd*-Na_2bpdc (Figure. 11). The amount of weight loss corresponded to one water molecule per molecular formula. The incorporation of water molecules in the structure of Na_2bpdc may depend on the reaction temperature as well as the type of solvent used.

Further, the structural similarity between *hyd*-Na_2bpdc and Na_2bpdc is indirectly supported by the TGA curves because they show the same thermal behavior except for the water loss in *hyd*-Na_2bpdc below 100 ^oC (Figure. 11). Although both *hyd*-Na_2bpdc and Na_2bpdc are decomposed at ca. 600 ^oC, Na_2bpdc did not show any weight loss around 100 ^oC indicating that this compound is not hydrated. On the other hand, NaHbpdc exhibited no weight loss around 100 ^oC, which is consistent with the single-crystal XRD data of NaHbpdc, which is not hydrated. The structure of NaHbpdc is rapidly decomposed above 300 ^oC. The lower thermal stability of NaHbpdc compared to *hyd*-Na_2bpdc and Na_2bpdc is attributed to the weak coordination between Na^+ ions and the carbonyl group of carboxylic acid (COOH) groups, which were not deprotonated. This indicates that a higher degree of deprotonation is required to improve the thermal stability of organic electrode materials.

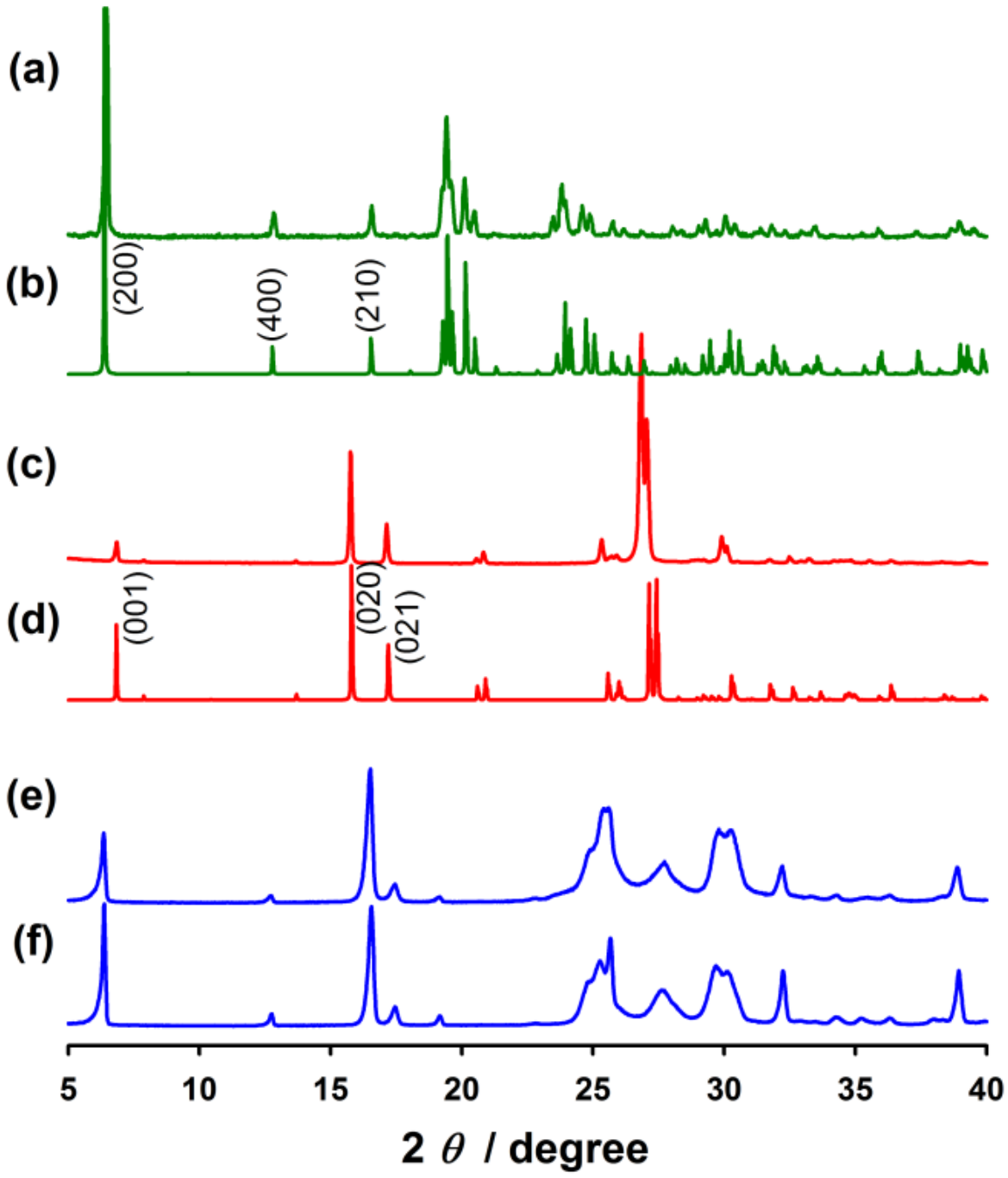

Figure. 10 PXRD patterns of (a) *hyd*-Na_2bpdc and (c) NaHbpdc, simulated patterns from single-crystal XRD data of (b) *hyd*-Na_2bpdc and (d) NaHbpdc, and PXRD patterns of (e) Na_2bpdc and (f) dehydrated hyd-Na_2bpdc dried at 120 °C.

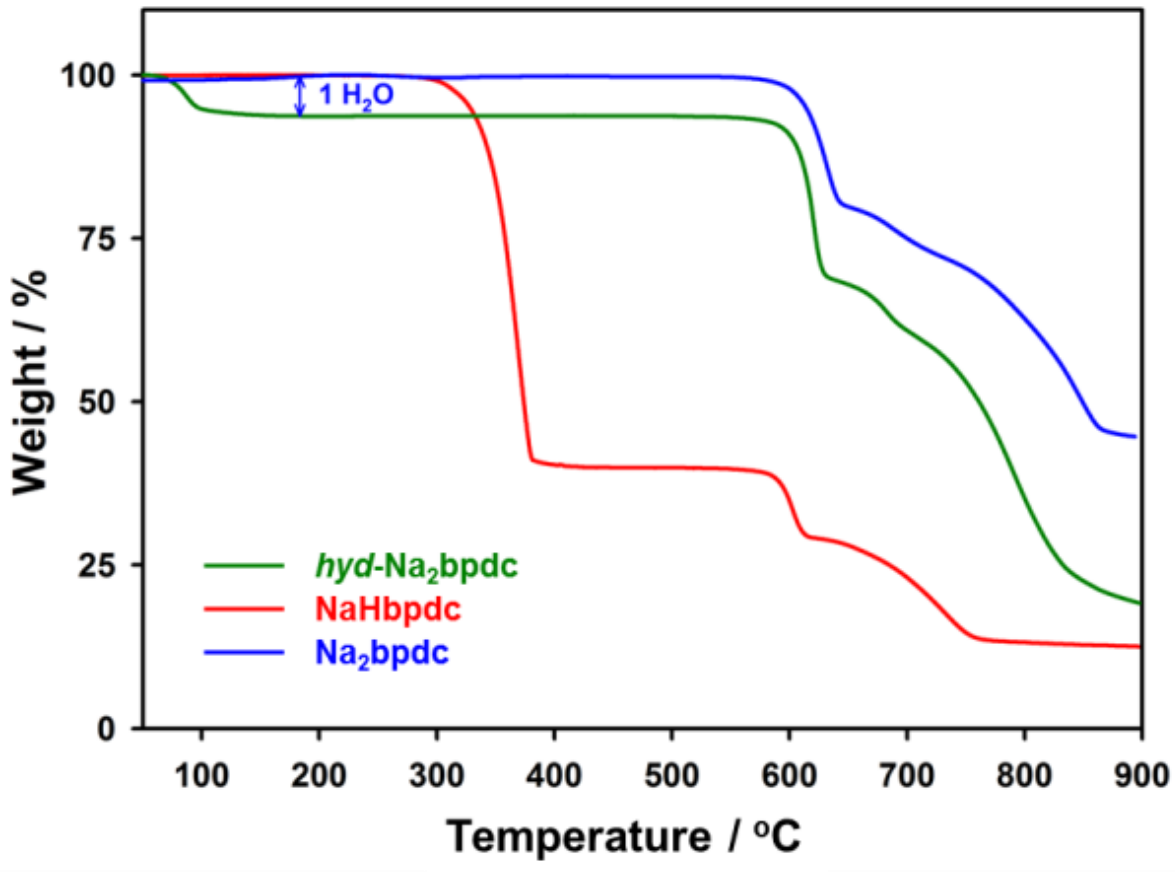

Figure. 11 TGA curves of *hyd*-Na_2bpdc, NaHbpdc, and Na_2bpdc.

The acid-base reactions of H_2bpdc with NaOH to produce *hyd*-Na_2bpdc, Na_2bpdc and NaHbpdc were further verified by Fourier transform infrared (FT-IR) spectroscopy. As shown in Figure. 12, the spectrum of H_2bpdc showed typical C=O stretching and O-H bending vibrations of carboxylic acid (COOH) groups at 1668 and 922 cm^{-1}, respectively. However, after the formation of the metal-carboxylate coordination (COO-Na) compounds via complete deprotonation by NaOH, the carbonyl (C=O) stretching vibration of the carboxylate groups (COO^-) in *hyd*-Na_2bpdc was shifted and split into two bands at 1579 and 1390 cm^{-1}, which were assigned as asymmetric (ν_{as}) and symmetric (ν_s) stretching vibrations, respectively (Figure. 12). Moreover, the characteristic O-H bending vibrations for the carboxylic acid groups around 920 cm^{-1} disappeared. The weak peak at 1690 cm^{-1} in the spectrum of *hyd*-Na_2bpdc corresponds to the O-H bending vibration of water. This observation agrees with the existence of guest water molecules, as suggested by single-crystal XRD and TGA data. Na_2bpdc showed the same FT-IR spectrum as *hyd*-Na_2bpdc, except for the peak around 1690 cm^{-1}. As expected from the XRD and TGA results, the FT-IR spectrum of NaHbpdc, containing both of the protonated and deprotonated form of carboxylic acid groups, showed peaks characteristic of both COOH and COO^- groups, i.e., C=O stretching and O-H bending vibrations of carboxylic acid at 1672 and 923 cm^{-1}, respectively, and ν_{as} and ν_s of the carboxylate groups at 1605 and 1399 cm^{-1}, respectively (Figure. 12).

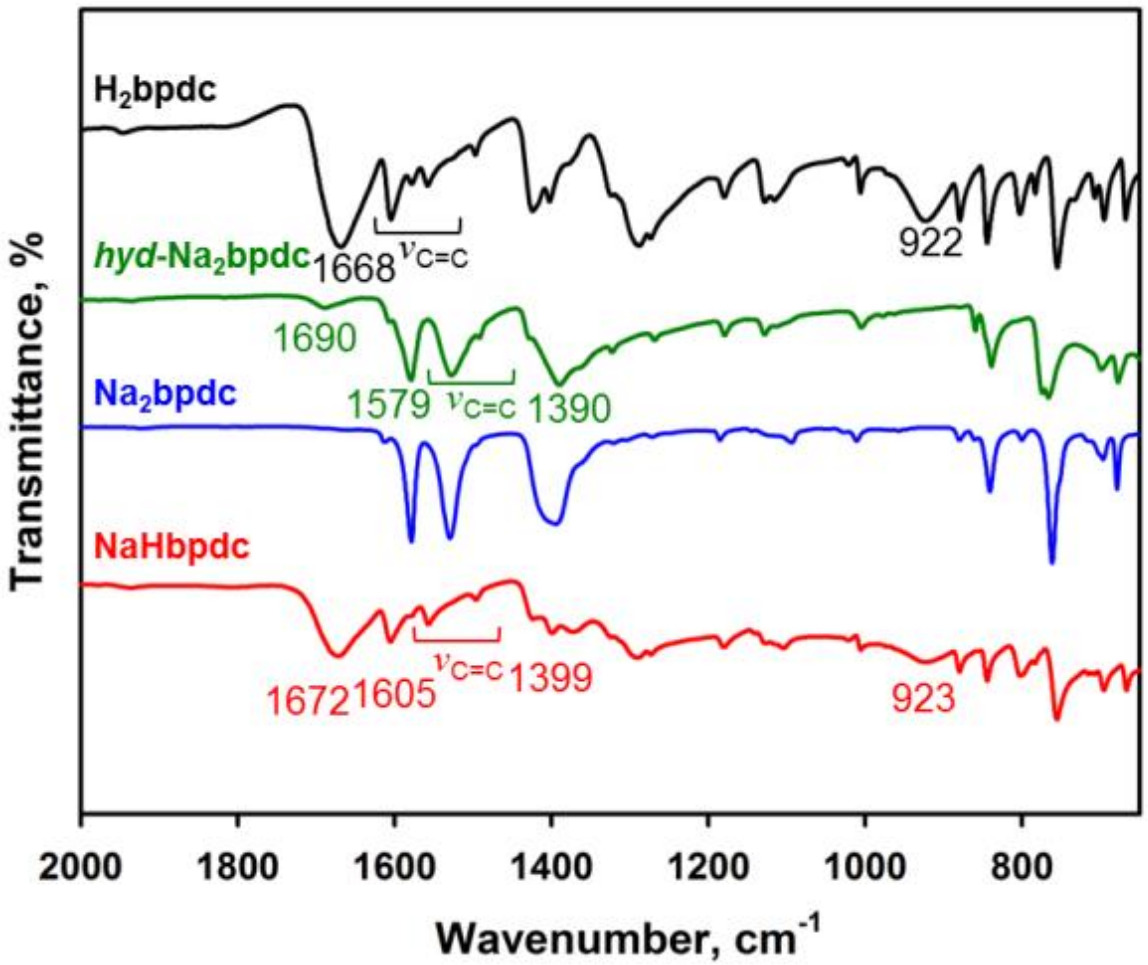

Figure. 12 FT-IR spectra of H_2bpdc, *hyd*-Na_2bpdc, Na_2bpdc and NaHbpdc; all the spectra were measured by using attenuated total reflectance (ATR) technique.

As shown in Figure. 13, Na_2bpdc and NaHbpdc, which have different crystal structures and degrees of deprotonation of the organic ligands, were examined as anode materials for Na-ion batteries. The cycle performance of *hyd*-Na_2bpdc was not examined separately because it transforms into Na_2bpdc during the preparation of the electrodes. The electrodes were dried at 120 ^{o}C under vacuum to remove the adsorbed water molecules on the surface of powders that is related to electrolyte decomposition during charging/discharging. This drying process leads to the dehydration of *hyd*-Na_2bpdc to afford Na_2bpdc. Both Na_2bpdc and NaHbpdc electrodes showed similar reversible capacities of approximately 200 mA h g^{-1} at ca. 0.5 V vs. Na/Na^+, which is larger than the theoretical specific capacity of 187 mA h g^{-1} corresponding two Na^+ ions storage, as shown in Scheme 1. The excess capacity (about 30 mA h g^{-1}) is attributed to carbon additive (super P) that can reversibly store Na^+ ions and delivers about 100 mA h g^{-1} (Fig. 14). The gravimetric specific capacity of bpdc-sodium salts is relatively small compared to other anode materials. Moreover, the densities of Na_2bpdc and NaHbpdc are 1.566 g cm^{-3} and 1.657 g cm^{-3}, respectively, based on X-ray single crystallographic data, which causes a low volumetric energy density. However, these organic electrode materials are cheap, indicating that organic electrode materials have an advantage of low cost/energy density. Above all, organic electrode materials are environmentally benign and reproducible, and this makes organic electrode materials attractive in spite of their relatively low energy density. Also, they showed a stable cycle performance of negligible capacity fading over 150 cycles. Notably, unlike Na_2bpdc, NaHbpdc showed a large amount of irreversible capacity at the first cycle. The coulombic efficiencies of Na_2bpdc and NaHbpdc at the first cycle were 81% and 47%, respectively. The poor coulombic efficiency of NaHbpdc (large sodiation capacity at the first cycle) is attributed to its irreversible electrolyte decomposition on the surface of NaHbpdc possessing carboxylic acid groups. The same behavior, i.e., a large amount of irreversible capacity at the first cycle, was also observed in a partially deprotonated monosodium terephthalate,[33] while a fully deprotonated disodium terephatalate showed good coulombic efficiency similar to Na_2bpdc.

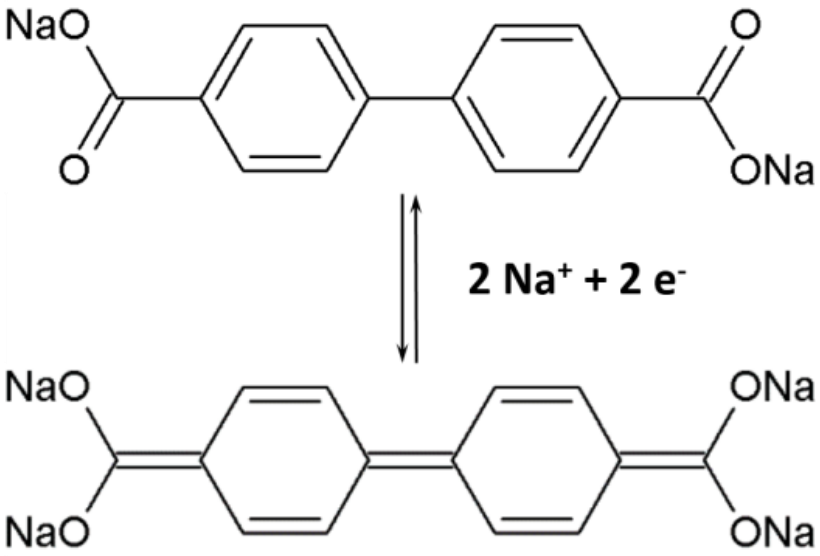

Scheme 1 Schematic diagram for the electrochemical redox reaction mechanism of Na_2bpdc.

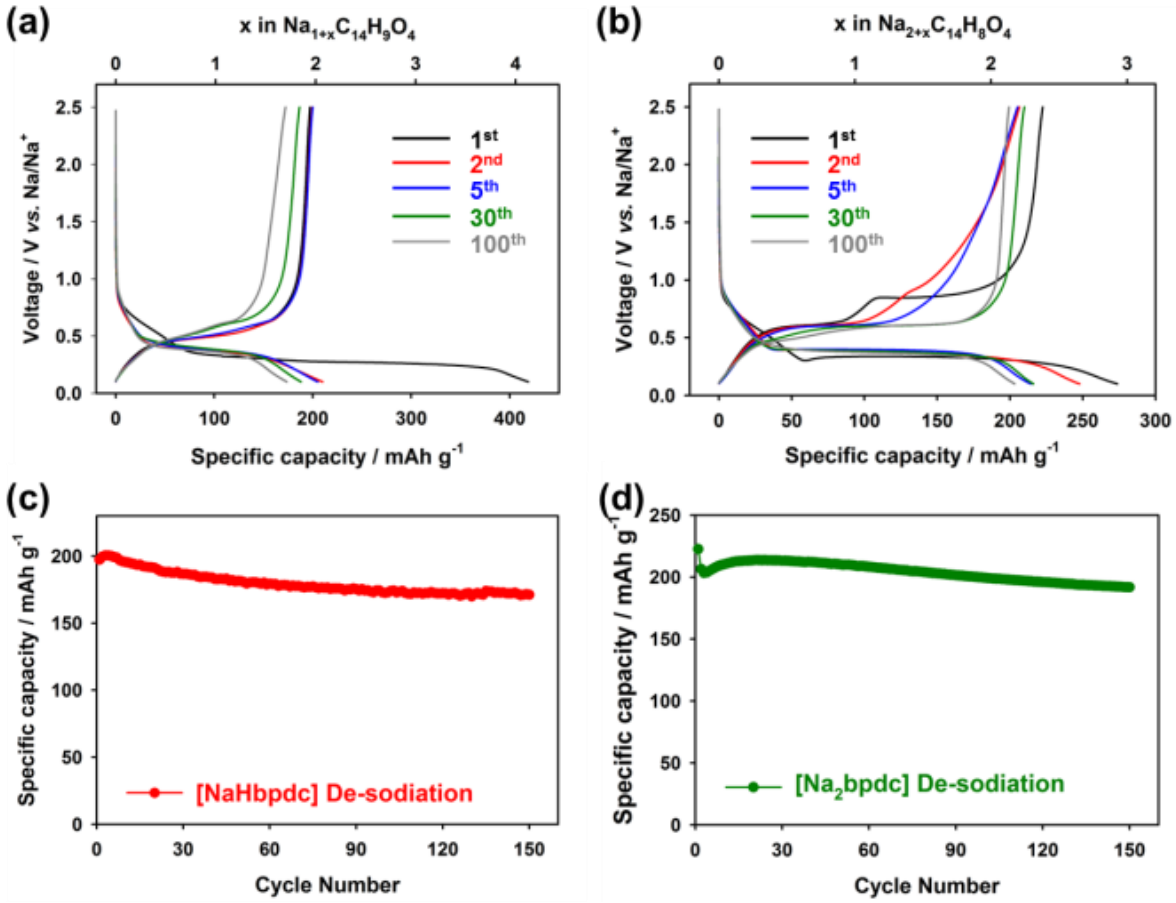

Figure. 13 Voltage profiles of (a) NaHbpdc and (b) Na_2bpdc; cycle performance of (c) NaHbpdc and (d) Na_2bpdc.

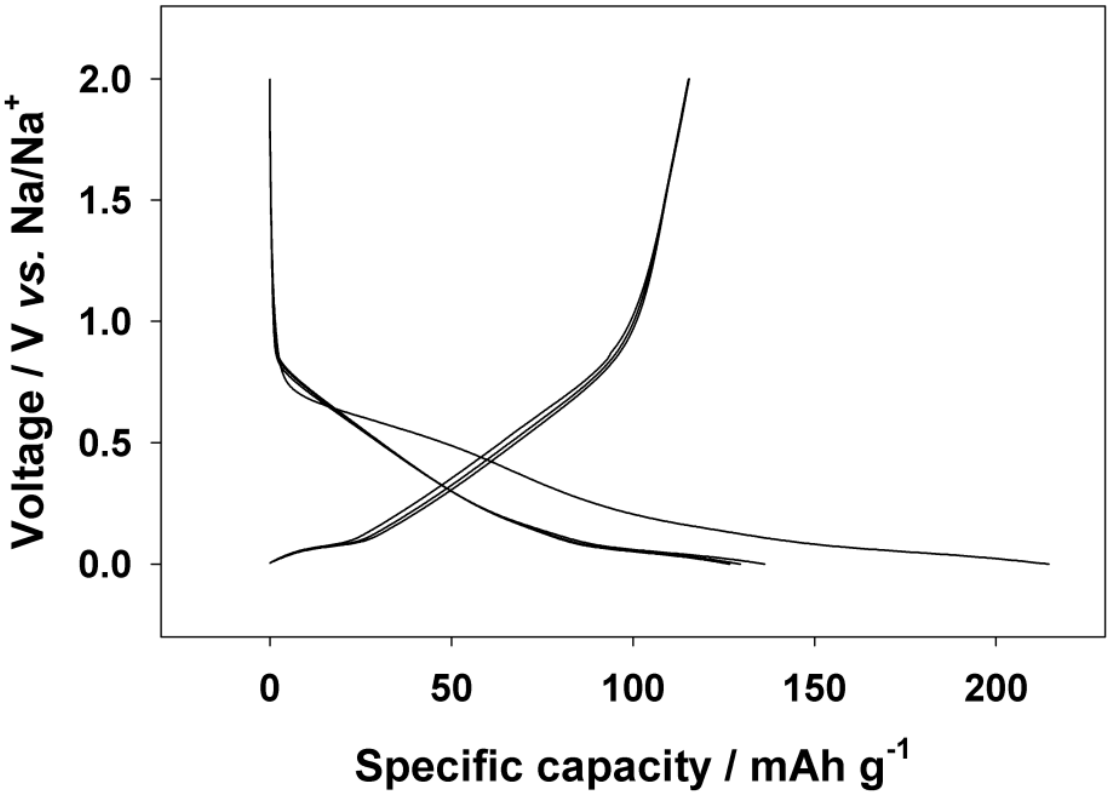

Figure 14. Voltage profiles of super P carbon.

The rate performances of Na_2bpdc and NaHbpdc were also compared, as shown in Figures. 15 and 16. Na_2bpdc showed a better rate performance than NaHbpdc, and even at a 20 C rate (3.74 A g^{-1}), Na_2bpdc sustained 50% of reversible capacity delivered at a 0.2 C rate. This superior rate performance of Na_2bpdc is definitely attributed to the smaller particle size (diffusion length) of Na_2bpdc compared to NaHbpdc, as shown in Figure. 17. The particle sizes of Na_2bpdc and NaHbpdc are a few μm and approximately 10 μm, respectively. However, even the dehydrated *hyd*-Na_2bpdc, which has a size similar to NaHbpdc, exhibited a better rate performance than NaHbpdc, indicating that the rate performance is affected by both the degree of deprotonation and the particle size of the bpdc-sodium salts. Electrodes with carboxylic groups cause a large amount of electrolyte decomposition, forming thick solid electrolyte interphase (SEI) layers, which result in the increase in polarization because of a large charge-transfer resistance. This is supported by the electrochemical impedance spectroscopy (EIS) analysis. The measurement was performed using the symmetric cells comprised of working electrode (bpdc salt)/working electrode (bpdc salt). The working electrodes were half-sodiated charging state after pre-cycling. As shown in Fig. 18, the semicircle of NaHbpdc is larger than that of *hyd*-Na_2bpdc, indicating that the charge-transfer resistance of NaHbpdc is larger than that of *hyd*-Na_2bpdc because the semicircle corresponds to charge-transfer resistance that is dependent on SEI layers. Moreover, while both the Na^+ cations present in the structure of Na_2bpdc can act as charge carriers for the solid state diffusion of Na^+ ions, the proton present in the structure of NaHbpdc cannot act as a charge carrier because it is strongly bound to the carbonyl group through covalent bonding. This indicates that the reduced amount of charge carriers in NaHbpdc compared to Na_2bpdc causes slower ionic diffusivity of Na^+ ions, resulting in poorer rate performance.

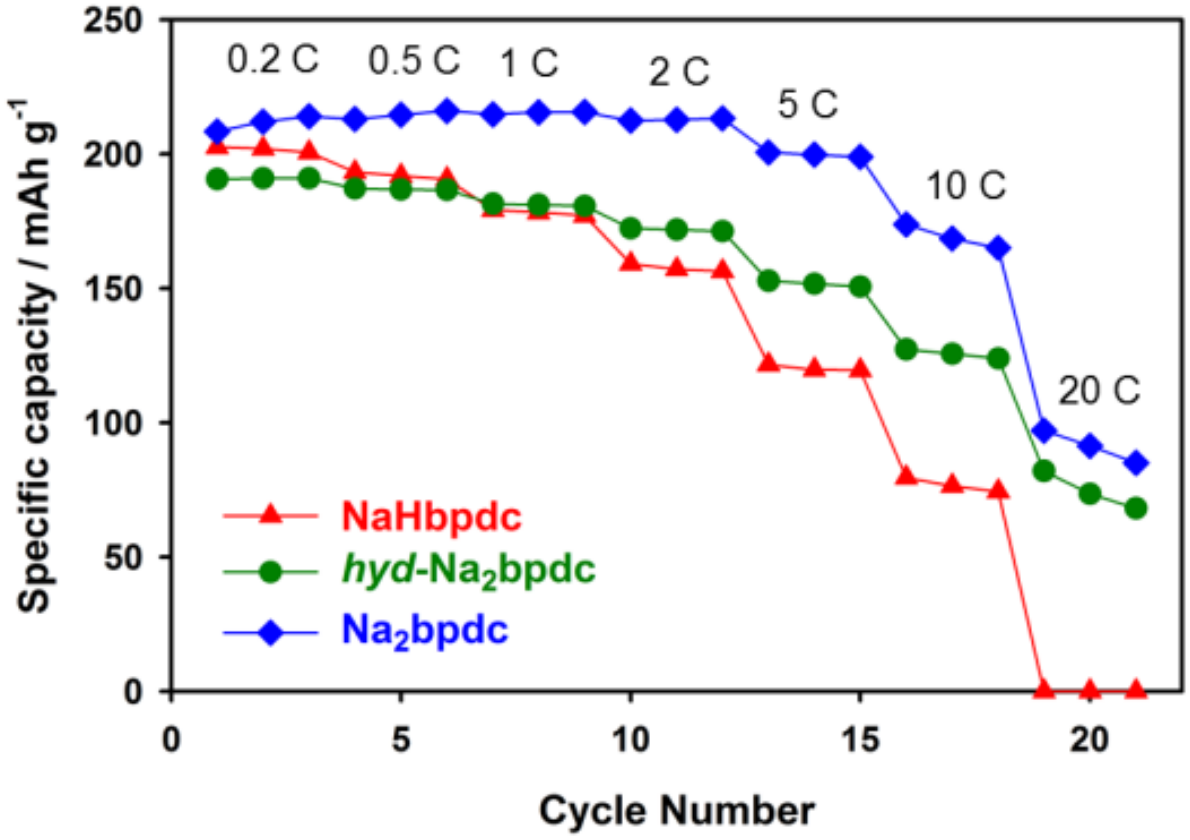

Figure. 15 Rate performance of *hyd*-Na_2bpdc, Na_2bpdc and NaHbpdc.

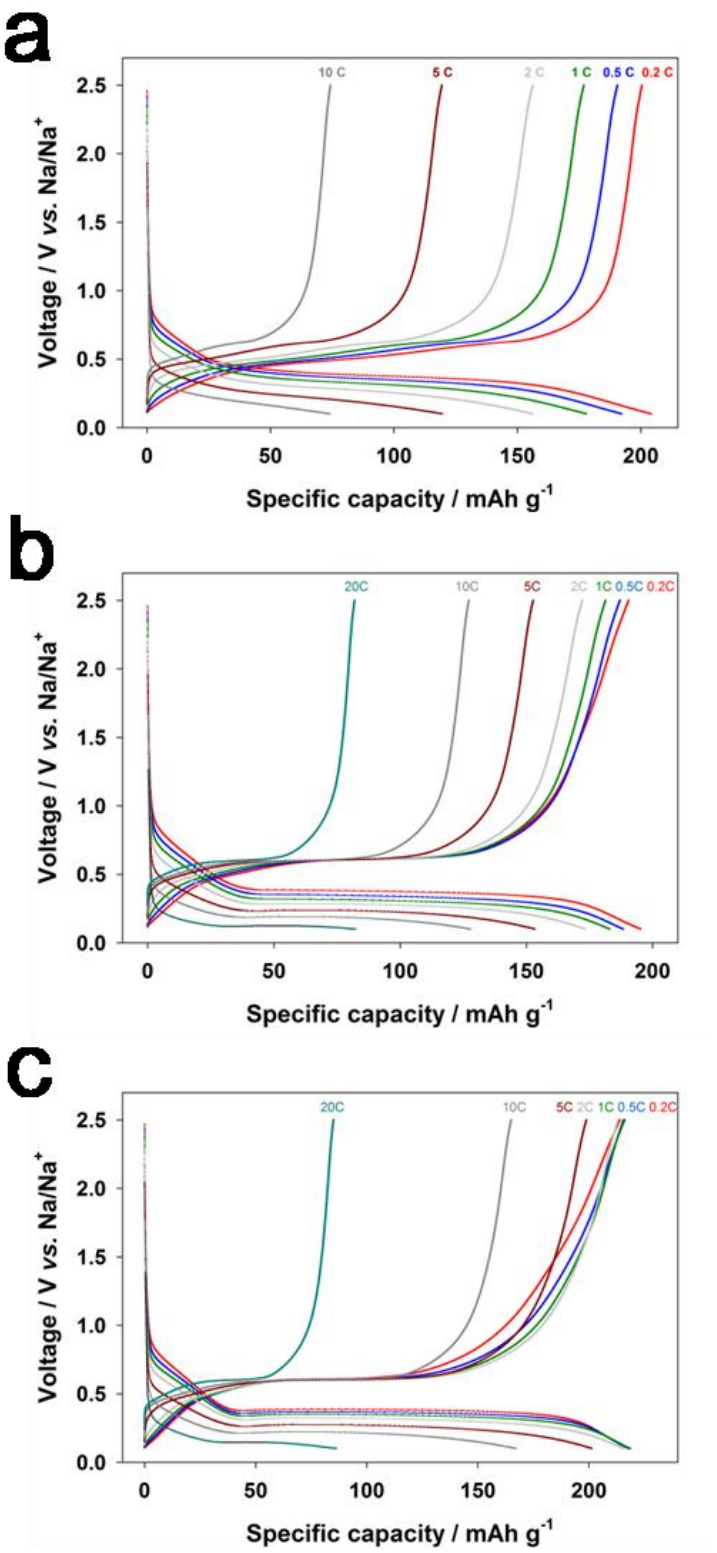

Figure 16. Rate performance of NaHbpdc, h-Na_2bpdc, and Na_2bpdc: voltage profiles of (a) NaHbpdc, (b) h-Na_2bpdc, and (c) Na_2bpdc.

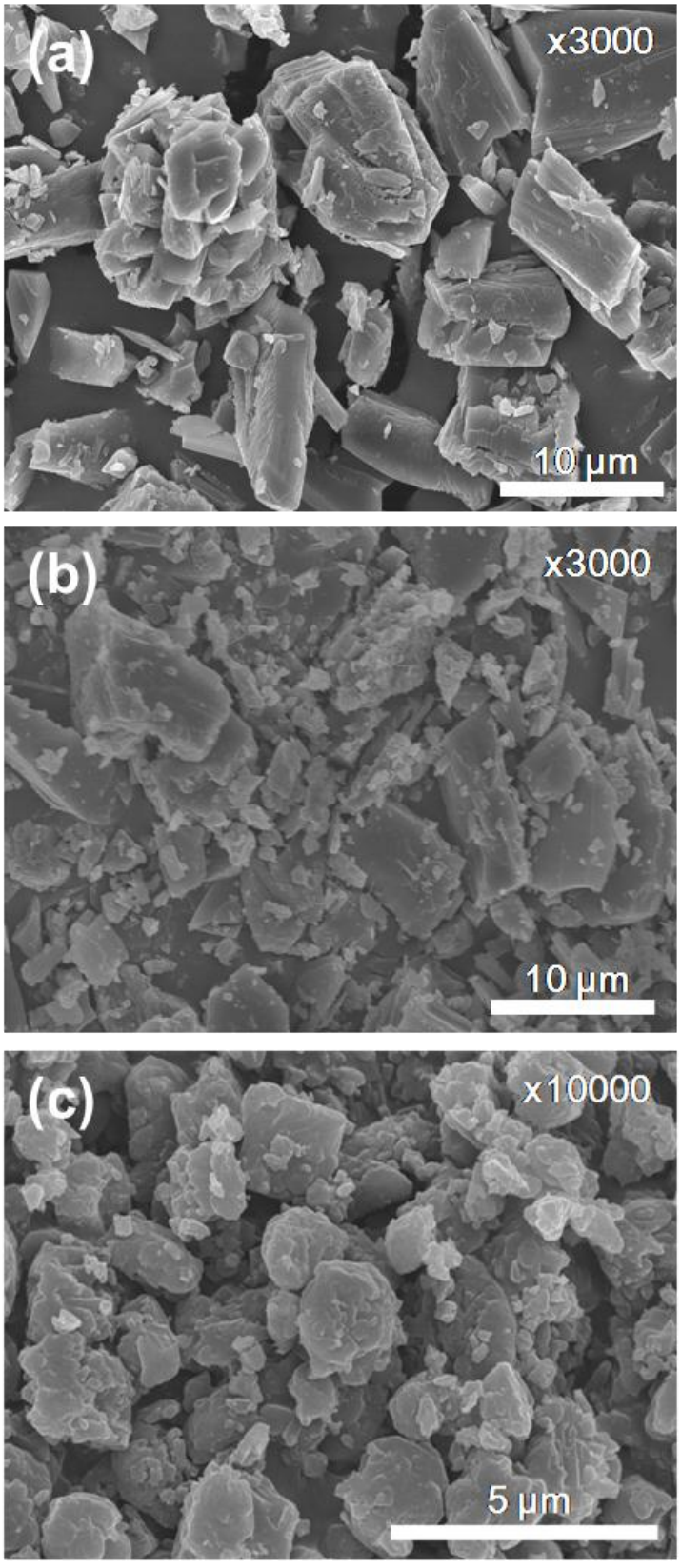

Figure. 17 SEM images of (a) NaHbpdc, (b) *hyd*-Na_2bpdc, and (c) Na_2bpdc

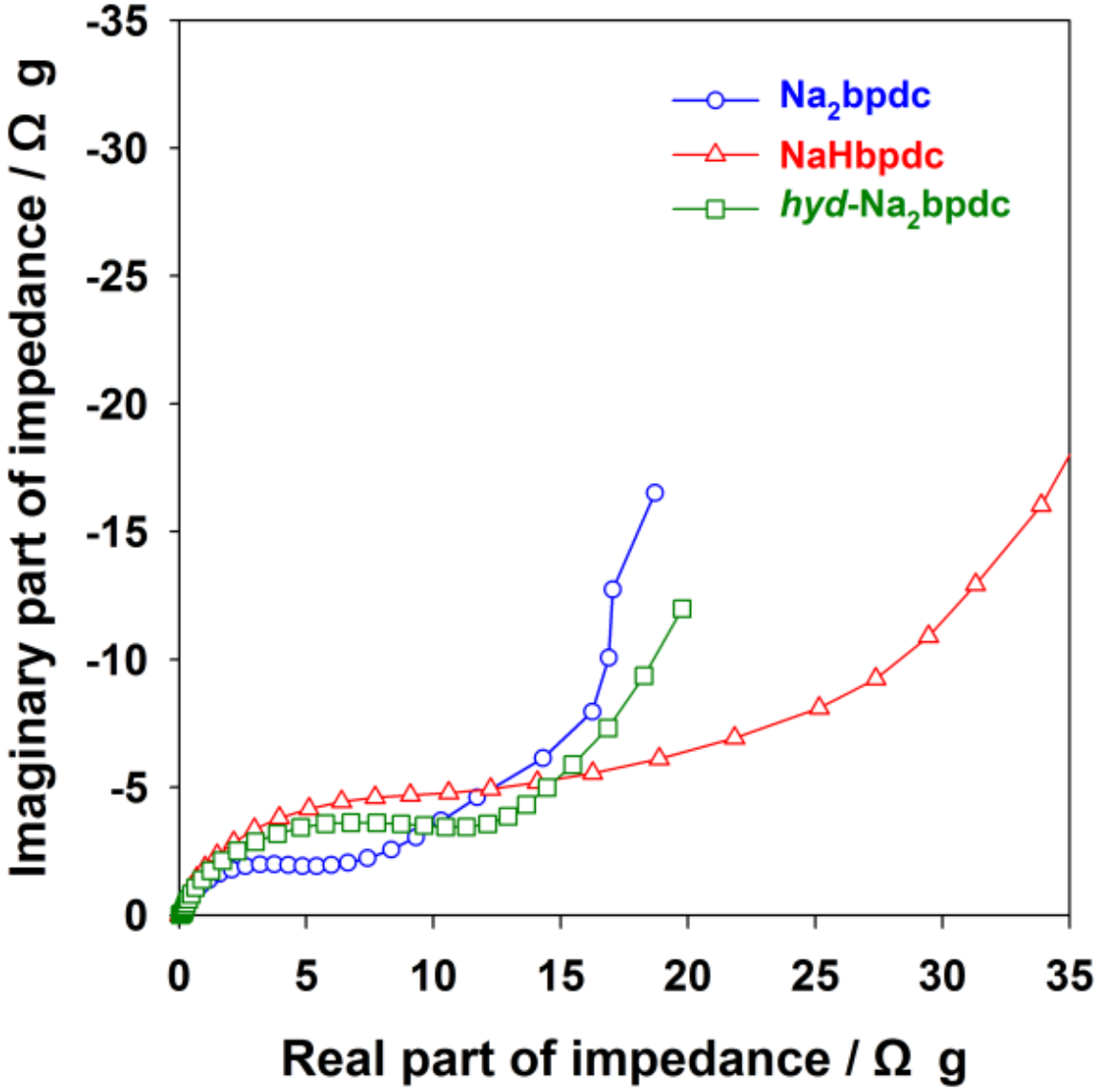

Fig. 18 Nyquist plots of bpdc electrode/bpdc electrode symmetric cells

To observe the structural changes upon sodiation/desodiation, *ex situ* XRD analysis of Na_2bpdc was performed, and it showed that the reversible sodiaiton/desodiation of Na_2bpdc proceeds in a two-phase reaction, as shown in Figure. 19. Upon sodiation, the intensity of PXRD peaks corresponding to Na_2bpdc decreased, and new peaks corresponding to the sodiated phase of Na_2bpdc gradually appeared at ca. 11, 20, 23 and 31^o (and vice versa for the desodiation). Despite two plateau steps in the voltage profile of desodiation during the first cycle, the *ex situ* XRD patterns showed that only one type of a two-phase reaction occurred during the desodiation. This agree well with the galvanostatic intermittent titration technique (GITT) curves, as shown in Figure. 20. Although two plateaus were observed during the first cycle, the second plateau is attributed to larger polarization because of a higher mass transfer resistance in Na-deficient compositions. This type of polarization behavior gradually disappeared on cycling, and may be closely related to the amorphization of Na_2bpdc during the cycling. As shown in the ex situ XRD patterns of the electrodes during cycling (Figure. 19c), broader PXRD peaks were observed after the cycling, indicating that the amorphization of Na_2bpdc occurred during cycling. In general, materials that are more amorphous show less polarization owing to the faster ionic diffusion at grain boundaries.

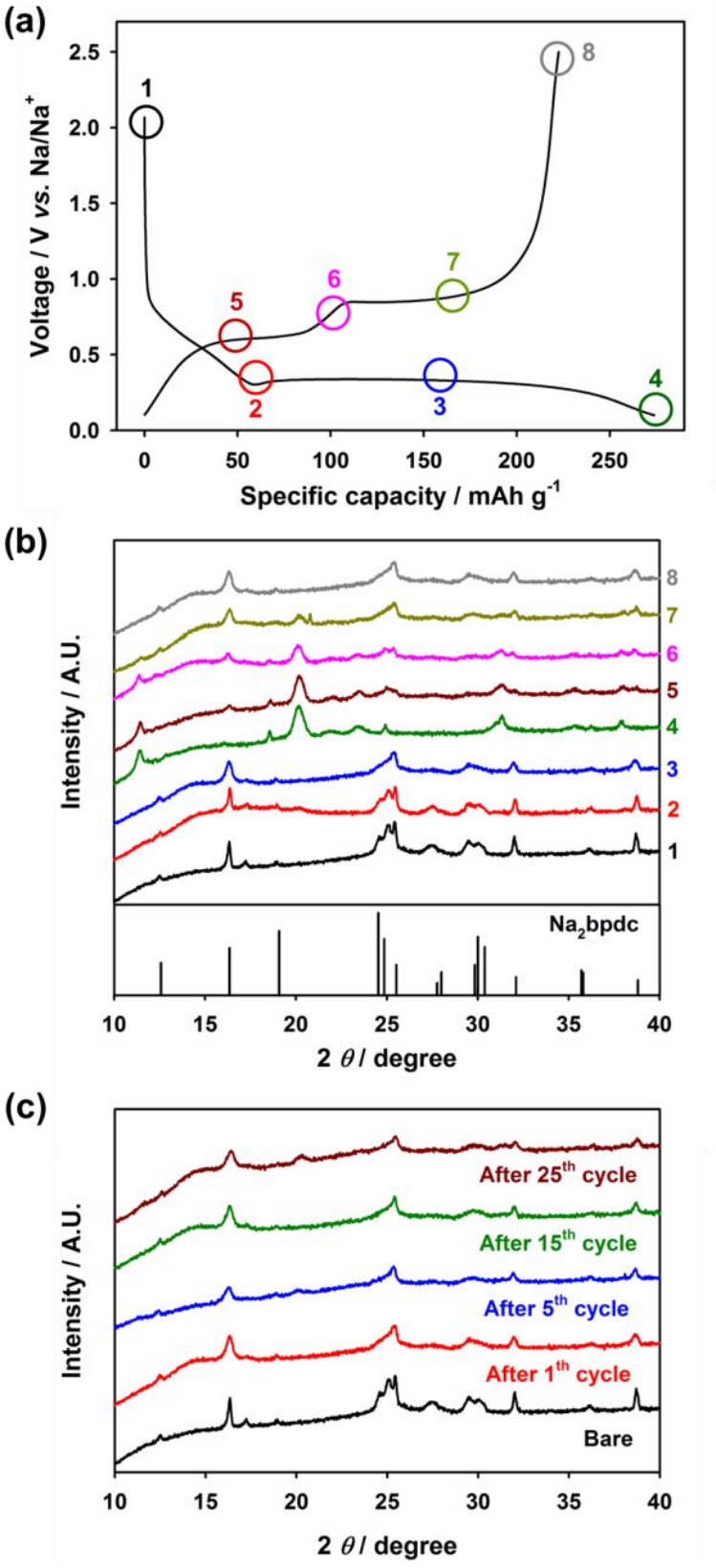

Figure. 19 *Ex situ* XRD analysis of Na_2bpdc: (a) voltage profiles, (b) corresponding XRD patterns, and (c) XRD patterns of desodiated electrodes during the various cyclings.

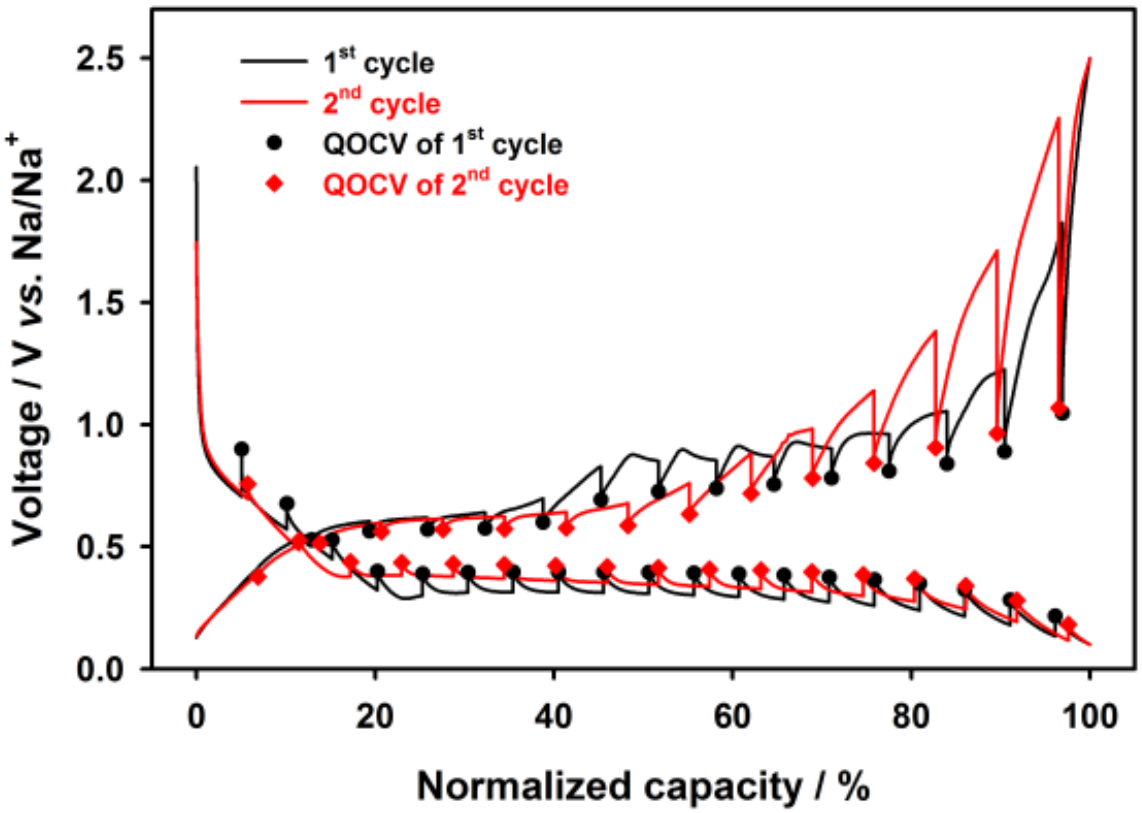

Figure. 20 GITT curves of Na_2bpdc.

Unlike Na_2bpdc, NaHbpdc showed an the irreversible phase transformation during the sodiation and desodiation, as shown in Figure. 21. NaHbpdc proceeds in a two-phase reaction during the sodiation and desodiation; however, the mixture phases of NaHbpdc and Na_2bpdc were observed after the desodiation. This indicates that the ion exchange occurred between the proton of carboxylic acid group in NaHbpdc and sodium ions in electrolytes during cycling. Similar behavior has been observed in the partially deprotonated monosodium terephthalate, which was transformed into the fully deprotonated disodium terephthalate due to the ion exchange between the proton and sodium during sodiation and desodiation.[33] The ion exchange of NaHbpdc powders was not observed when NaHbpdc powders were stored in electrolytes for 3, 5, and 10 days without passage of current, as shown in Fig. 22, and thus, the ion exchange is merely related to electrochemical sodiation and desodiation.

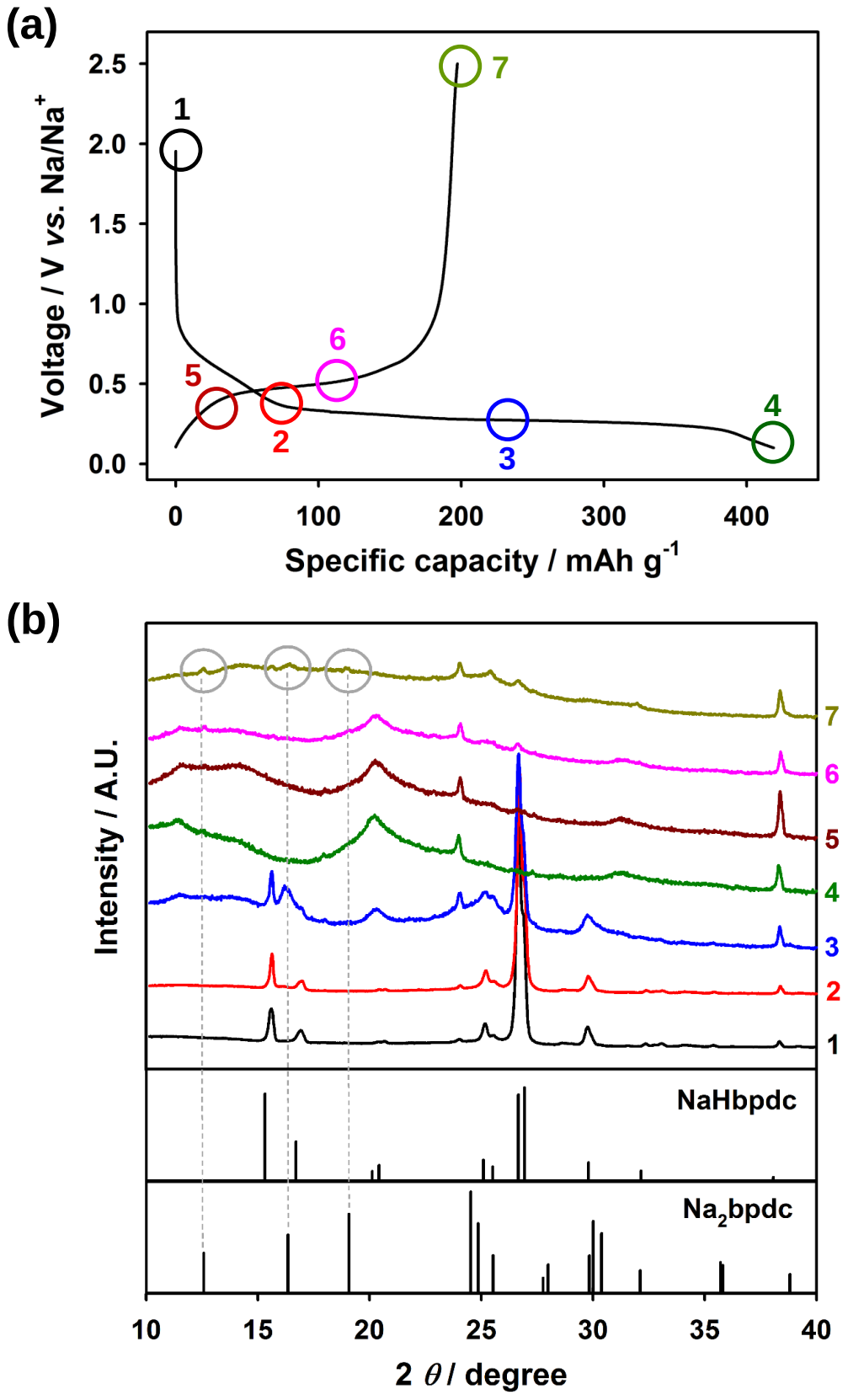

Figure. 21 *Ex situ* XRD analysis of NaHbpdc: (a) voltage profiles and (b) corresponding XRD patterns.

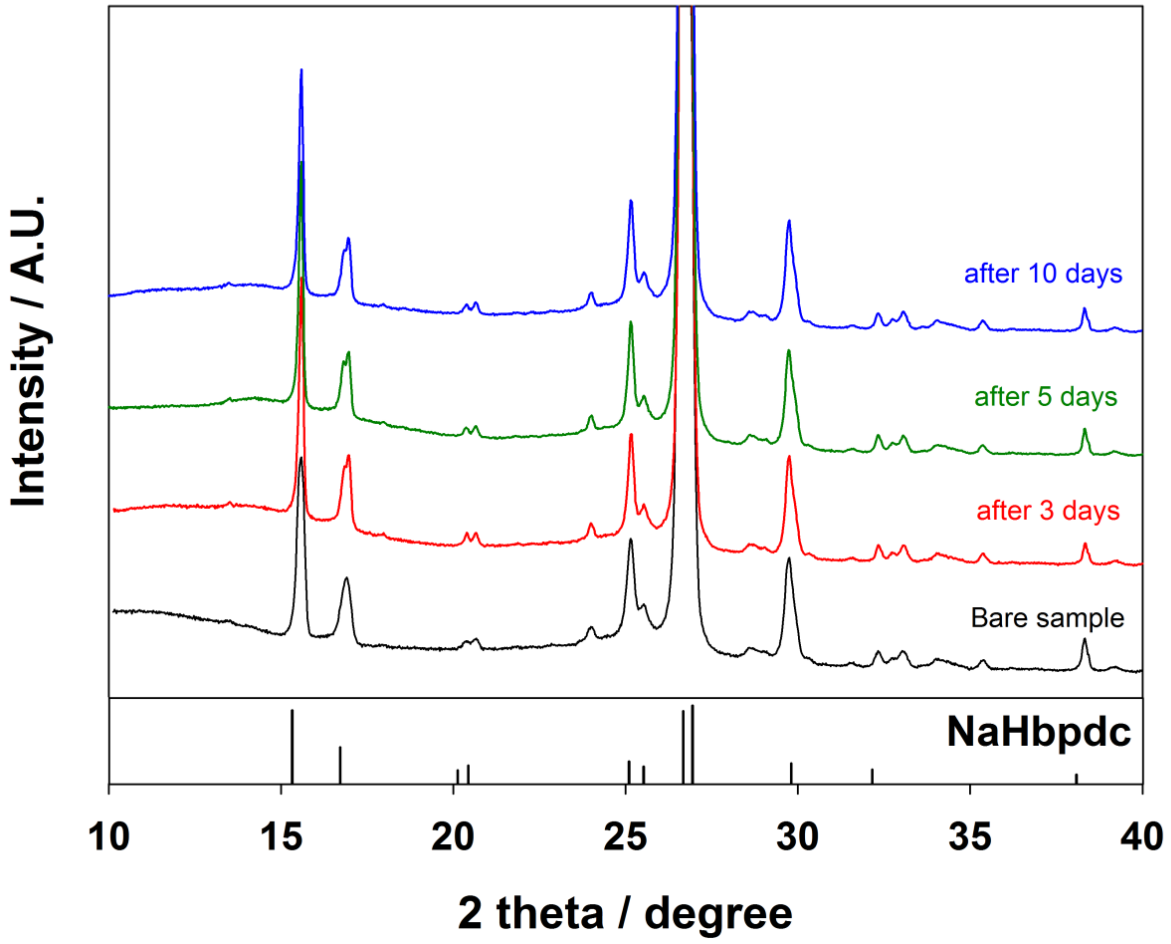

Figure 22. XRD patterns of NaHbpdc powders after storage in electrolytes for 3, 5, and 10 days.

4. Conclusion

In conclusion, the crystal structures and electrochemical performance of bpdc-sodium salts as anode materials for Na-ion batteries have been evaluated for the first time. The different degrees of deprotonation and differently coordinated water molecules in the bpdc-sodium salts were obtained through deliberate synthesis such as precipitation and solvothermal methods, resulting in the formation of bpdc-sodium salts with three different crystal structures. Their crystal structures were determined using single-crystal XRD. The bpdc-sodium salts exhibited a promising electrochemical performance with a reversible capacity of 220 mA h g^{-1} at ca. 0.5 V vs. Na/Na^{+}, negligible capacity fading over 150 cycles, and an excellent rate performance of approximately 100 mA h g^{-1} even at a 20 C rate. The sodiation/desodiation of bpdc-sodium salts proceeds in a two-phase reaction. In addition, the degree of deprotonation in bpdc-sodium salts not only affected the electrochemical performance, but also affected the corresponding reaction mechanisms. The fully deprotonated bpdc-disodium salt (Na_2bpdc) showed better coulombic efficiency and rate performance than the partially deprotonated bpdc-monosodium salt (NaHbpdc). Unlike Na_2bpdc, which showed reversible phase transition during sodiation and desodiation, NaHbpdc exhibited an irreversible phase transition during the cycling.

References

1. Armand, M.; Tarascon, J. M., Building better batteries. *Nature* **2008,** *451* (7179), 652-657.

2. Ellis, B. L.; Lee, K. T.; Nazar, L. F., Positive Electrode Materials for Li-Ion and Li-Batteries†. *Chemistry of Materials* **2010,** *22* (3), 691-714.

3. Goodenough, J. B.; Park, K.-S., The Li-Ion Rechargeable Battery: A Perspective. *Journal of the American Chemical Society* **2013,** *135* (4), 1167-1176.

4. Tarascon, J. M.; Armand, M., Issues and challenges facing rechargeable lithium batteries. *Nature* **2001,** *414* (6861), 359-367.

5. Whittingham, M. S., Lithium batteries and cathode materials. *Chemical Reviews* **2004,** *104* (10), 4271-4302.

6. Dunn, B.; Kamath, H.; Tarascon, J.-M., Electrical energy storage for the grid: A battery of choices. *Science* **2011,** *334* (6058), 928-935.

7. Ellis, B. L.; Nazar, L. F., Sodium and sodium-ion energy storage batteries. *Current Opinion in Solid State and Materials Science* **2012,** *16* (4), 168-177.

8. Stevens, D.; Dahn, J., The mechanisms of lithium and sodium insertion in carbon materials. *Journal of The Electrochemical Society* **2001,** *148* (8), A803-A811.

9. Lee, K. T.; Hong, S. Y.; Kim, Y.; won Park, Y.; Choi, A.; Choi, N.-S., Charge Carrier in Rechargeable Batteries: Na ions vs. Li ions. *Energy Environ. Sci.* **2013**.

10. Komaba, S.; Murata, W.; Ishikawa, T.; Yabuuchi, N.; Ozeki, T.; Nakayama, T.; Ogata, A.; Gotoh, K.; Fujiwara, K., Electrochemical Na Insertion and Solid Electrolyte Interphase for Hard-Carbon Electrodes and Application to Na-Ion Batteries. *Advanced Functional Materials* **2011,** *21* (20), 3859-3867.

11. Liang, Y.; Tao, Z.; Chen, J., Organic electrode materials for rechargeable lithium batteries. *Advanced Energy Materials* **2012,** *2* (7), 742-769.

12. Armand, M.; Grugeon, S.; Vezin, H.; Laruelle, S.; Ribière, P.; Poizot, P.; Tarascon, J.-M., Conjugated dicarboxylate anodes for Li-ion batteries. *Nature materials* **2009,** *8* (2), 120-125.

13. Shao, Y. Y.; Xiao, J.; Wang, W.; Engelhard, M.; Chen, X. L.; Nie, Z. M.; Gu, M.; Saraf, L. V.; Exarhos, G.; Zhang, J. G.; Liu, J., Surface-Driven Sodium Ion Energy Storage in Nanocellular Carbon Foams. *Nano Lett.* **2013,** *13* (8), 3909-3914.

14. Cao, Y. L.; Xiao, L. F.; Sushko, M. L.; Wang, W.; Schwenzer, B.; Xiao, J.; Nie, Z. M.; Saraf, L. V.; Yang, Z. G.; Liu, J., Sodium Ion Insertion in Hollow Carbon Nanowires for Battery Applications. *Nano Lett.* **2012,** *12* (7), 3783-3787.

15. Xu, Y. H.; Zhu, Y. J.; Liu, Y. H.; Wang, C. S., Electrochemical Performance of Porous Carbon/Tin Composite Anodes for Sodium-Ion and Lithium-Ion Batteries. *Adv. Energy Mater.* **2013,** *3* (1), 128-133.

16. Darwiche, A.; Marino, C.; Sougrati, M. T.; Fraisse, B.; Stievano, L.; Monconduit, L., Better Cycling Performances of Bulk Sb in Na-Ion Batteries Compared to Li-Ion Systems: An Unexpected Electrochemical Mechanism. *J. Am. Chem. Soc.* **2012,** *134* (51), 20805-20811.

17. Baggetto, L.; Allcorn, E.; Manthiram, A.; Veith, G. M., Cu2Sb thin films as anode for Na-ion batteries. *Electrochem. Commun.* **2013,** *27*, 168-171.

18. Zhu, H. L.; Jia, Z.; Chen, Y. C.; Weadock, N.; Wan, J. Y.; Vaaland, O.; Han, X. G.; Li, T.; Hu, L. B., Tin Anode for Sodium-Ion Batteries Using Natural Wood Fiber as a Mechanical Buffer and Electrolyte Reservoir. *Nano Lett.* **2013,** *13* (7), 3093-3100.

19. Wang, Y. S.; Yu, X. Q.; Xu, S. Y.; Bai, J. M.; Xiao, R. J.; Hu, Y. S.; Li, H.; Yang, X. Q.; Chen, L. Q.; Huang, X. J., A zero-strain layered metal oxide as the negative electrode for long-life sodium-ion batteries. *Nat. Commun.* **2013,** *4*.

20. Senguttuvan, P.; Rousse, G.; Seznec, V.; Tarascon, J. M.; Palacin, M. R., Na2Ti3O7: Lowest Voltage Ever Reported Oxide Insertion Electrode for Sodium Ion Batteries. *Chem. Mat.* **2011,** *23* (18), 4109-4111.

21. Sun, Q.; Ren, Q. Q.; Li, H.; Fu, Z. W., High capacity Sb2O4 thin film electrodes for rechargeable sodium battery. *Electrochem. Commun.* **2011,** *13* (12), 1462-1464.

22. Sun, Y.; Zhao, L.; Pan, H. L.; Lu, X.; Gu, L.; Hu, Y. S.; Li, H.; Armand, M.; Ikuhara, Y.; Chen, L. Q.; Huang, X. J., Direct atomic-scale confirmation of three-phase storage mechanism in Li4Ti5O12 anodes for room-temperature sodium-ion batteries. *Nat. Commun.* **2013,** *4*.

23. Woo, S. H.; Park, Y.; Choi, W. Y.; Choi, N. S.; Nam, S.; Park, B.; Lee, K. T., Trigonal Na4Ti5O12 Phase as an Intercalation Host for Rechargeable Batteries. *J. Electrochem. Soc.* **2012,** *159* (12), A2016-A2023.

24. Kim, Y.; Park, Y.; Choi, A.; Choi, N. S.; Kim, J.; Lee, J.; Ryu, J. H.; Oh, S. M.; Lee, K. T., An Amorphous Red Phosphorus/Carbon Composite as a Promising Anode Material for Sodium Ion Batteries. *Adv. Mater.* **2013,** *25* (22), 3045-3049.

25. Qian, J. F.; Wu, X. Y.; Cao, Y. L.; Ai, X. P.; Yang, H. X., High Capacity and Rate Capability of Amorphous Phosphorus for Sodium Ion Batteries. *Angew. Chem.-Int. Edit.* **2013,** *52* (17), 4633-4636.

26. Liang, Y.; Tao, Z.; Chen, J., Organic Electrode Materials for Rechargeable Lithium Batteries. *Adv. Energy Mater.* **2012,** *2* (7), 742-769.

27. Geng, J.; Bonnet, J.-P.; Renault, S.; Dolhem, F.; Poizot, P., Evaluation of polyketones with N-cyclic structure as electrode material for electrochemical energy storage: case of tetraketopiperazine unit. *Energy Environ. Sci.* **2010,** *3* (12), 1929.

28. Han, X.; Qing, G.; Sun, J.; Sun, T., How many lithium ions can be inserted onto fused C6 aromatic ring systems? *Angewandte Chemie* **2012,** *51* (21), 5147-51.

29. Liang, Y.; Zhang, P.; Chen, J., Function-oriented design of conjugated carbonyl compound electrodes for high energy lithium batteries. *Chemical Science* **2013,** *4* (3), 1330.

30. Morita, Y.; Nishida, S.; Murata, T.; Moriguchi, M.; Ueda, A.; Satoh, M.; Arifuku, K.; Sato, K.; Takui, T., Organic tailored batteries materials using stable open-shell molecules with degenerate frontier orbitals. *Nature materials* **2011,** *10* (12), 947-51.

31. Park, Y.; Shin, D. S.; Woo, S. H.; Choi, N. S.; Shin, K. H.; Oh, S. M.; Lee, K. T.; Hong, S. Y., Sodium terephthalate as an organic anode material for sodium ion batteries. *Adv Mater* **2012,** *24* (26), 3562-7.

32. Zhao, L.; Zhao, J. M.; Hu, Y. S.; Li, H.; Zhou, Z. B.; Armand, M.; Chen, L. Q., Disodium Terephthalate (Na2C8H4O4) as High Performance Anode Material for Low-Cost Room-Temperature Sodium-Ion Battery. *Adv. Energy Mater.* **2012,** *2* (8), 962-965.

33. Abouimrane, A.; Weng, W.; Eltayeb, H.; Cui, Y. J.; Niklas, J.; Poluektov, O.; Amine, K., Sodium insertion in carboxylate based materials and their application in 3.6 V full sodium cells. *Energy Environ. Sci.* **2012,** *5* (11), 9632-9638.

34. Sakaushi, K.; Hosono, E.; Nickerl, G.; Gemming, T.; Zhou, H.; Kaskel, S.; Eckert, J., Aromatic porous-honeycomb electrodes for a sodium-organic energy storage device. *Nat Commun* **2013,** *4*, 1485.